

AD-A265 874



FORMATION PAGE

Form Approved

OMB No. 0704-0188

2

to average 1 hour per response, including the time for reviewing instructions, searching existing data sources, gathering the collection of information. Send comments regarding this burden estimate or any other aspect of this collection of information, including suggestions for reducing this burden, to Washington Headquarters Services, Directorate for Information Operations and Reports, 1215 Jefferson Davis Highway, Suite 1204, Arlington, VA 22202-4302, and to the Office of Management and Budget, Paperwork Reduction Project (0704-0188), Washington, DC 20503.

1. AGENCY USE ONLY (Leave blank)	2. REPORT DATE 6-10-93	3. REPORT TYPE AND DATES COVERED Annual 4/15/92 - 4/14/93	
4. TITLE AND SUBTITLE Polarimetric Passive Remote Sensing of Ocean Surface		5. FUNDING NUMBERS N00014-92-J-1616 4215043-01	
6. AUTHOR(S) Prof. J.A. Kong		8. PERFORMING ORGANIZATION REPORT NUMBER	
7. PERFORMING ORGANIZATION NAME(S) AND ADDRESS(ES) Research Laboratory of Electronics Massachusetts Institute of Technology 77 Massachusetts Avenue Cambridge, MA 02139		10. SPONSORING / MONITORING REPORT NUMBER	
9. SPONSORING / MONITORING AGENCY NAME(S) AND ADDRESS(ES) Office of Naval Research 800 North Quincy Street Arlington, VA 22217-5000		11. SUPPLEMENTARY NOTES The view, opinions and/or findings contained in this report are those of the author(s) and should not be construed as an official Department of the Army position, policy, or decision, unless so designated by other documentation.	
12a. DISTRIBUTION / AVAILABILITY STATEMENT Approved for public release; distribution unlimited.		12b. DISTRIBUTION CODE	
13. ABSTRACT (Maximum 200 words) Work by Prof. Kong and his collaborators is summarized here			
14. SUBJECT TERMS		15. NUMBER OF PAGES	
		16. PRICE CODE	
17. SECURITY CLASSIFICATION OF REPORT UNCLASSIFIED	18. SECURITY CLASSIFICATION OF THIS PAGE UNCLASSIFIED	19. SECURITY CLASSIFICATION OF ABSTRACT UNCLASSIFIED	20. LIMITATION OF ABSTRACT UL

ANNUAL REPORT

Title: POLARIMETRIC PASSIVE REMOTE SENSING OF OCEAN SURFACE

Sponsor by: Department of the Navy
Office of Naval Research

Contract number: N00014-92-J-1616

Research Organization: Center for Electromagnetic Theory and Applications
Research Laboratory of Electronics
Massachusetts Institute of Technology

OSP number: 76989

Principal Investigator: J. A. Kong

Period covered: April 15, 1992 - April 14, 1993

Accession For	
NTIS CRA&I	<input checked="" type="checkbox"/>
DTIC TAB	<input type="checkbox"/>
Unannounced	<input type="checkbox"/>
Justification	
By	
Distribution /	
Availability Codes	
Dist	Avail and/or Special
A-1	

ALL QUALITY INSPECTED a.

93-13413



93 6 15 115

POLARIMETRIC PASSIVE REMOTE SENSING OF OCEAN SURFACE

Under the sponsorship of the ONR Contract Contract N00014-92-J-1616 we have published 4 refereed journal and conference papers.

Update of progress in "Polarimetric Passive Remote Sensing of Ocean Surfaces"

Our work on this project in the past year has concentrated primarily on the phase one goals as outlined in the original proposal. To date, we have performed an experiment in which the polarimetric thermal emission from a sinusoidal water surface was measured and compared against a theoretical model, performed a study of the polarimetric thermal emission from surfaces randomly rough in one direction, and begun work on a model for predicting the polarimetric thermal emission from surfaces randomly rough in two directions. Each of these studies is described in more detail below.

Polarimetric Thermal Emission from a Sinusoidal Water Surface

To verify further our earlier findings reported in [1,2] for ocean-like surfaces, an experiment was designed and carried out in which the polarimetric thermal emission from a sinusoidal water surface was measured [3,4]. This sinusoidal water surface was created by placing a thin sheet of fiberglass with a sinusoidal profile on top of a pool of water and removing the air trapped underneath the fiberglass layer. The resulting surface was actually a 'two-layer' periodic surface whose thermal emission should be close to that of a true sinusoidal water surface if the effect of the fiberglass layer is neglected. The first three Stokes parameters of the thermal emission were measured at both 10 GHz and 14 GHz using a linearly polarized radiometer whose polarization basis was rotated to perform the polarimetric measurements. Significant values of the brightness temperature corresponding to the third Stokes parameter U were observed at various polar and azimuthal angles (as high as 40 K for certain configurations). A theoretical model for the thermal emission from such a two-layer periodic surface was constructed, and its predictions agreed well with the experimental measurements. This theoretical model also indicated that the fiberglass layer

did slightly affect the brightness temperatures in horizontal and vertical polarizations, but had a much smaller effect on U .

Polarimetric Thermal Emission from Surfaces Randomly Rough in One Direction

Our experiment indicated that appreciable values of U could be obtained from a periodic sinusoidal water surface. However, an actual wind generated ocean surface has a very complicated structure and can only be described statistically as a random process. Thus, a numerical experiment in which the polarimetric thermal emission from randomly rough surfaces was investigated was next performed [5].

Many approximate theories, such as the Kirchhoff approximation and the small perturbation method, exist for use in predicting the thermal emission from randomly rough surfaces. However, the theoretical predictions of [1] indicate that large surface slopes are needed to obtain appreciable values of U . Since the approximate theories mentioned above are known to fail if the surface slopes become too large, a Monte Carlo approach was chosen for the study.

In this method, a set of surface profiles in two dimensions with given statistics was generated using a spectral method. The profiles obtained were extended infinitely in the third direction. The thermal emission from each surface of the set was then calculated using an exact integral equation approach. The results from the set were averaged to obtain the Monte Carlo estimate of the polarimetric thermal emission. The surfaces generated were intended to model the ocean in the microwave frequency range. For this purpose, a power law spectrum was chosen for the surface statistics. The surface profiles generated were also made periodic to avoid problems with edge conditions in the calculations. Convergence of the results with both the period of the surface chosen and the number of surface profiles averaged was investigated in the study. The results of the study indicate that U also exists for randomly rough surfaces and indicates the direction of the surface periodicity. U was also found to be sensitive to the rms height of the surface and power law spectrum slope, and insensitive to the polar angle, permittivity of the surface medium, and high frequency content of the surface spectra beyond a certain cutoff.

Polarimetric Thermal Emission from Surfaces Randomly Rough in Two Directions

The preceeding Monte Carlo study gave some indications as to the properties that the third Stokes brightness parameter, U , could be expected to possess for a randomly rough surface. However, the effect of a two directional roughness spectrum on the U predictions is not yet known. For this purpose, we are currently working on a model for calculating the polarimetric thermal emission for a surface rough in two directions. A Monte Carlo study using this model is also proposed to ascertain the properties of the U parameter for this more accurate ocean surface model. This model is based on modification of the extended boundary condition approach that was used for the previous Monte Carlo study, and the surface statistics to be used will model both the upwind and crosswind components of the ocean wave spectrum.

Summary

The success of these studies in measuring and theoretically predicting the properties of the third brightness parameter, U , have advanced the idea of using U as an indicator of ocean wind direction from remotely sensed data. Our work in the development of a model and algorithm for the realization of such a goal will continue as planned.

Polarimetric thermal emission from rough surfaces (J. T. Johnson, J. A. Kong, R. T. Shin, D. H. Staelin, S. H. Yueh, S. V. Nghiem, R. Kwok, K. O'Neill, and A. Lohanick), submitted to *Progress in Electromagnetics Research Symposium*, California Institute of Technology, Pasadena, California, July 12-16, 1993.

Polarimetric thermal emission from rough ocean surfaces: a numerical study (J. T. Johnson, J. A. Kong, R. T. Shin, S. H. Yueh, S. V. Nghiem, and R. Kwok), *Applied Computational Electromagnetics Symposium*, Monterey, California, March 22-26, 1993.

Polarimetric Thermal Emission from Rough Ocean Surfaces (J. T. Johnson, J. A. Kong, R. T. Shin, S. H. Yueh, S. V. Nghiem, and R. Kwok), submitted to *J. Electromag. Waves Applic.*, , 1993.

Third Stokes parameter emission from a periodic water surface (J. T. Johnson, J. A. Kong, R. T. Shin, D. H. Staelin, K. O'Neill, and A. Lohanick), accepted for publication on the *IEEE Trans. Geosci. and Remote Sens.*, 1992.

REFERENCES

1. Veysoglu, M. E., H. A. Yueh, R. T. Shin and J. A. Kong, "Polarimetric passive remote sensing of periodic surfaces," *J. Electromag. Waves Applic.*, Vol. 5, No. 3, 267-280, 1991.
2. Nghiem, S. V., M. E. Veysoglu, J. A. Kong, R. T. Shin, K. O'Neill, and A. W. Lohanick, "Polarimetric passive remote sensing of a periodic soil surface: microwave measurements and analysis," *J. Electromag. Waves Applic.*, Vol. 5, No. 9, 997-1005, 1991.
3. Johnson, J. T., J. A. Kong, R. T. Shin, D. H. Staelin, K. O'Neill, and A. Lohanick, "Third Stokes parameter emission from a periodic water surface," submitted to *IEEE Trans. Geosci. and Remote Sens.*, 1992.
4. Yueh, S. H., S. V. Nghiem, W. Wilson, R. Kwok, F. K. Li, J. T. Johnson, and J. A. Kong, "Polarimetric thermal emission from periodic water surfaces," submitted to *Radio Science*, 1992.
5. Johnson, J. T., J. A. Kong, R. T. Shin, S. H. Yueh, S. V. Nghiem, and R. Kwok, "Polarimetric Thermal Emission from Rough Ocean Surfaces," submitted to *J. Electromag. Waves Applic.*, , 1993.

Polarimetric Thermal Emission from Rough Surfaces

J. T. Johnson, J. A. Kong, R. T. Shin, and D. H. Staelin
Department of Electrical Engineering and Computer Science
and Research Laboratory of Electronics
Massachusetts Institute of Technology, Cambridge, MA

S. H. Yueh, S. V. Nghiem, and R. Kwok
Jet Propulsion Laboratory
California Institute of Technology, Pasadena, CA

K. O'Neill and A. Lohanick
Cold Regions Research and Engineering Laboratory, Hanover, NH

Recent theoretical works have suggested the potential of passive polarimetry in the remote sensing of geophysical media. It has been shown the third Stokes parameter U of the thermal emission may become large for azimuthally asymmetric fields of observation. In order to investigate the potential applicability of passive polarimetry to the remote sensing of ocean surface, measurements of the polarimetric thermal emission from a sinusoidal water surface and a numerical study of the polarimetric thermal emission from randomly rough ocean surfaces were performed.

Measurements of sinusoidal water surface thermal emission were performed using a sinusoidal water surface which was created by placing a thin sheet of fiberglass with a sinusoidal profile in two dimensions extended infinitely in the third dimension onto a water surface. The theory of thermal emission from a "two-layer" periodic surface is derived and the exact solution is performed using both the extended boundary condition method (EBC) and the method of moments (MOM). The theoretical predictions are found to be in good agreement with the experimental results once the effects of the radiometer antenna pattern are included and the contribution of background noise to the measurements is modeled. The experimental results show that the U parameter indicates the direction of periodicity of the water surface and can approach values of up to 30 K for the surface observed.

Next, a numerical study of polarimetric thermal emission from randomly rough surfaces was performed. A Monte Carlo technique utilizing an exact method for calculating thermal emission was chosen for the study to avoid any of the limitations of the commonly used approximate methods in rough surface scattering. In this Monte Carlo technique, a set of finite rough surface profiles in two dimensions with desired statistics was generated and extended periodically. The polarimetric thermal emission from each surface of the set was then calculated using both the EBC and the MOM and the results were averaged. The surface statistics chosen were intended to model a wind perturbed ocean surface in the X to K_u band microwave region.

The results of the study indicate that the U parameter is sensitive to the azimuthal angle between the surface periodicity and the looking angle and to the rms height of the surface, and that the U parameter is fairly insensitive to variations in polar angle, permittivity, surface power law spectrum, and surface spectrum high frequency cutoff. These properties give further strength to the idea of using the U parameter to detect wind direction over the ocean.

Polarimetric Thermal Emission from Rough Ocean Surfaces: A Numerical Study

J. T. Johnson, J. A. Kong, and R. T. Shin
Department of Electrical Engineering and Computer Science
and Research Laboratory of Electronics
Massachusetts Institute of Technology, Cambridge, MA

S. H. Yueh, S. V. Nghiem, and R. Kwok
Jet Propulsion Laboratory
California Institute of Technology, Pasadena, CA

Abstract A numerical study of the polarimetric thermal emission from ocean surfaces randomly rough in one dimension using a Monte Carlo technique is presented. In this study, a set of finite length surface profiles with desired statistics was generated using a spectral method. Each surface was extended periodically to create an infinite rough surface, and the thermal emission was computed using the extended boundary condition method (EBC) and the method of moments (MOM). The results from the set of surfaces were then averaged to obtain the Monte Carlo estimate of polarimetric thermal emission. The surface statistics chosen were intended to model a wind perturbed ocean surface in the X to K_u band microwave region. The results of the study show that the third Stokes parameter, U_B , is sensitive to the azimuthal angle between the surface periodicity and the looking angle, the rms height of the surface, and the surface power law spectrum slope, and that this parameter is insensitive to variations in polar angle, permittivity, and surface spectrum high frequency content as an indicator of the azimuthal asymmetry of the surface.

1 Introduction

Recent theoretical works have suggested the potential of passive polarimetry in the remote sensing of geophysical media [1-5]. It has been shown that the brightness temperature in the third Stokes parameter, U_B , may become large for azimuthally asymmetric fields of observation. In references [4] and [5], values of U_B as high as 30 K were measured from sinusoidal water surfaces at 10 and 14.6 GHz. In order to investigate the potential applicability of passive polarimetry to the remote sensing of rough ocean surfaces, a numerical study of the polarimetric thermal emission from ocean surfaces randomly rough in one dimension was performed. A Monte Carlo technique utilizing an exact integral equation method for calculating thermal emission was chosen for the study.

The next section presents a brief background on the theory of polarimetry and describes the passive polarimetric brightness vector. The method of calculation for the numerical experiment is discussed in Section 3 and the numerical results are presented in Section 4.

2 Theory of Polarimetry

In passive polarimetry, brightness temperatures corresponding to all of the four modified Stokes parameters are measured. The brightness temperature Stokes vector is defined as

$$\bar{T}_B = \frac{1}{C} \bar{I} = \frac{1}{C} \begin{bmatrix} I_h \\ I_v \\ U \\ V \end{bmatrix} = \frac{1}{\eta C} \begin{bmatrix} \langle E_h E_h^* \rangle \\ \langle E_v E_v^* \rangle \\ 2\text{Re}\langle E_v E_h^* \rangle \\ 2\text{Im}\langle E_v E_h^* \rangle \end{bmatrix} \quad (1)$$

where E_h and E_v are the emitted electric fields received from the horizontal and vertical polarization channels of the radiometer, η is the characteristic impedance, and $C = K/\lambda^2$ with K denoting Boltzmann's constant, λ the wavelength. The first two parameters of the brightness temperature Stokes vector correspond to the powers received in the horizontal and vertical polarization channels, respectively. The third and fourth parameters correspond to the complex correlation between the electric fields received by the horizontal and vertical channels. We will label the four parameters T_{Bh} , T_{Bv} , U_B , and V_B respectively in this paper. It is shown in [3] that the third and fourth Stokes parameters may be related to the brightness temperature in a 45 degree linearly polarized measurement (T_{Bl}) and a right hand circularly polarized measurement (T_{Br}) as follows:

$$U_B = 2T_{Bl} - T_{Bh} - T_{Bv} \quad (2)$$

$$V_B = 2T_{Br} - T_{Bh} - T_{Bv} \quad (3)$$

Thus, to calculate all four parameters of the brightness temperature Stokes vector, the brightness temperatures in horizontal, vertical, 45 degree linear, and right hand circular polarizations are first calculated, and the above equations are used to obtain U_B and V_B .

In the passive remote sensing of rough surfaces, the parameter that is actually of interest is the emissivity, which relates the brightness temperature emitted by an object to its actual physical temperature, under the assumption that the object is at a constant physical temperature and that the emission from the object is the only source of brightness:

$$T_{Ba} = e_a(\theta, \phi) T_{phys} \quad (4)$$

In the above equation, the subscript a refers to the polarization of the brightness temperature, θ to the polar observation angle, and ϕ to the azimuthal observation angle. Through the principles of energy conservation and reciprocity, Kirchhoff's law relates this emissivity to the reflectivity of the surface [6]:

$$e_a(\theta, \phi) = 1 - r_a(\theta, \phi) \quad (5)$$

The reflectivity $r_a(\theta, \phi)$ for the given incident polarization a is defined as the fraction of the power incident from direction (θ, ϕ) that is rescattered and can be evaluated by

integrating the bistatic scattering coefficient $\gamma_{ba}(\theta, \phi; \theta', \phi')$ over all scattering angles in the upper hemisphere and summing the results of both orthogonal scattering polarizations.

$$r_a(\theta, \phi) = \frac{1}{4\pi} \sum_b \int_0^{\pi/2} d\theta' \sin \theta' \int_0^{2\pi} d\phi' \gamma_{ba}(\theta, \phi; \theta', \phi') \quad (6)$$

In the above expression, (θ, ϕ) and (θ', ϕ') represent the incident and the scattered directions, respectively, and the subscripts a and b represent the polarizations of the incident and the scattered waves, respectively.

Thus, to calculate the fully polarimetric emission vector, the bistatic scattering coefficient for each of four polarizations is first calculated and integrated over the upper hemisphere to obtain the reflectivity for that particular polarization. Multiplication of the corresponding emissivity by the physical temperature of the object under view yields the brightness temperature for this polarization. The fully polarimetric brightness vector is then calculated as described previously. A physical temperature of 300 K was assumed for the surfaces in this experiment.

3 Method of Calculation

Scattering from randomly rough surfaces has been studied extensively by a number of researchers. Numerous approximate techniques, such as the Kirchhoff approximation and the small perturbation method, exist and work well under certain restrictions for providing the statistically expected values of scattered fields and power [6]. However, it was found in [2] that in order to measure large U_B values from a sinusoidal surface, a large height to period ratio was required. The large slopes of such a surface fall into the regions of non-applicability for the above methods, so a Monte Carlo method was chosen for the study.

In this Monte Carlo method, a set of surface profiles with given statistics was generated, and the fully polarimetric brightness vector from each surface was calculated using an exact integral equation approach. The results for the set were then averaged to obtain the final Monte Carlo estimate of the average brightness vector for those particular surface parameters. The surface generation and analysis procedure are described in more detail in the next section.

3.1 Random Surface Generation

A spectral method, described in [7-8], was used to generate a finite sample of a rough surface with desired statistics. In this method, a set of normally distributed (both real and imaginary part) Fourier coefficients is generated and then weighted by a spectral density function in the frequency domain. The resulting Fourier coefficients are then transformed back into the space domain using an inverse FFT algorithm to obtain a surface profile

sampled in space. The surface profiles were linearly interpolated between the specified points.

Since only a finite surface profile could be generated, an infinite surface was created by extending this finite surface periodically. The Floquet modes obtained from the periodic surface are thus a discrete approximation to the continuous spectrum of a truly infinite random rough surface. The effect of this periodic extension on the polarimetric brightness temperature was investigated by comparing the results from a set of surfaces with a given period with the results from a set of surfaces a longer period and the same frequency spectrum. A period of 20 wavelengths was found to be sufficient to provide convergence of the U_B results to within 0.3 K for longer period surfaces. The surfaces were continuous when made periodic due to the periodic properties of the FFT series from which they were generated.

The surface profiles generated were rough in one dimension only due to the complexity of the calculations for surfaces rough in two spatial directions. The rough profile along the x direction was extended infinitely along the y direction in the calculations (see Figure 1). Three dimensional angles of incidence were allowed, however, so that polarimetric effects could be observed from the resulting 'conical diffraction' problem. While this model is extremely simple when compared to an actual wind perturbed ocean surface, its results should give some indication as to the properties of U_B for general rough surfaces.

The surface statistics chosen for the calculations were intended to model ocean surfaces in the microwave frequency range. For this purpose, a dielectric constant of $50 + i30$ was chosen for the medium and a power-law spectral density function for the surfaces was used. This function, $\phi(k)$ is described by:

$$\phi(k) = \begin{cases} k^{-s} & \frac{2\pi}{5\lambda} \leq k \leq k_c \\ 0 & \text{otherwise} \end{cases} \quad (7)$$

where k is the spatial wavenumber of the surface in rad/m , s is the slope of the power law spectrum, and k_c is the cutoff wavenumber of the surface set. The effects of varying the slope of the spectrum and its high frequency cutoff were investigated in the experiment. The surface in Figure 1 is one of the surfaces generated with -3 slope power law spectrum and a high frequency cutoff of $k_c = 4\pi/\lambda$.

Each surface was normalized independently of the others to a specified rms surface height: rms heights of $\lambda/20$, $\lambda/25$ and $\lambda/30$ were chosen to investigate the effect of varying the surface height on the polarimetric brightness temperature. The 20λ requirement for the surface period prevents larger rms heights from being studied due to computational limitations. Each generated surface consisted of 400 points within this period, so that the surface profile was sampled every $\lambda/20$ along the x direction. This sampling frequency is well above all of the Nyquist frequencies of the power spectral density functions used in the experiment. The surface statistics calculated from the generated surface sets were compared to their desired theoretical values and found to be in good agreement.

The results from ten surface profiles were averaged for all of the points in the exper-

iment. The convergence of the results with the number of surface profiles averaged was investigated by comparing the results from independent groups of ten surfaces. The results for U_B were found to be within 0.2 K.

3.2 Integral Equation Method

Numerous studies have been made of scattering from a periodic surface. The Extended Boundary Condition (EBC) method [9] is one of the most efficient methods, but has been found to become ill conditioned for steep surfaces. The Method of Moments (MOM) for a periodic surface, described in [2], is another solution of the problem that does not have the steep surface problems of the EBC, but is more computationally intensive. The calculations from these two methods were compared for a sample surface for each case in the experiment and found to give similar results in all of the cases. This agreement indicates that the surface slope limitations of the EBC were not exceeded, and this more efficient method of calculation was used for the larger surface sets of the experiment.

4 Results of Calculations

Figure 2 is a plot of the average U_B value for the $\lambda/20$, $\lambda/25$, and $\lambda/30$ rms height surfaces as a function of azimuthal angle for a polar angle of 20 degrees. A power law slope of -3 , cutoff wavenumber of $k_c = 4\pi/\lambda$, and dielectric constant of $50 + i30$ were used. Points were calculated every 15 deg in azimuthal angle, so that the interpolating lines shown should not be taken to be exact. It is seen that the U_B value is small for viewing angles parallel or perpendicular to the direction of periodicity of the surface, and that the highest values of U_B are obtained at azimuthal angles of approximately 45 or 135 degrees. The magnitude of U_B is determined by the rms height of the surface, with rougher surfaces giving higher values. The small values of U_B obtained in these results (2 K) are due to the convergence requirements for the Monte Carlo technique: larger U_B values could be obtained by analyzing rougher surfaces, but would require more computer time than was available for this study. Also, data collected from the SSM/I and reported by Wentz [10] indicates that the azimuthal variation in T_{Bh} and T_{Bv} for real wind perturbed ocean surfaces at both 37 and 19 GHz is typically less than 3 K, as is obtained for these rms heights. The U_B channel is seen to indicate the azimuthal direction of the surface in all cases where it is observable. Note that negative values for U_B are possible, as this parameter corresponds only to a correlation between real observables. Also, the symmetry about $\phi = 90$ deg seen in Figure 2 and the following figures is due only to the statistical symmetry of the surface set about this angle; individual surfaces are not symmetric about $\phi = 90$ deg. This gives an indication that the average of the ten surface profiles is converging to the true statistical average.

Figure 3 investigates the effects of polar angle on the U_B . Plotted are the results at polar angles of 20, 40, and 50 degrees for the $\lambda/20$ rms height, -3 slope, $k_c = 4\pi/\lambda$,

50 + i30 dielectric constant surfaces. The results are surprisingly similar, demonstrating that this parameter is relatively insensitive to polar angle as an indicator of surface azimuthal direction. These larger polar angles are important due to the need for large polar angles in satellite borne sensor applications.

Figure 4 illustrates the effect of permittivity on U_B . Results for polar angle 20 degrees, rms height $\lambda/20$, -3 slope, $k_c = 4\pi/\lambda$, and dielectric constants of 40 + i25, 50 + i30, and 60 + i35 are plotted. The results again indicate that the U_B channel is insensitive to a change in the dielectric constant around 50 + i30.

Figure 5 displays the variation in U_B with the slope of the power law spectrum, s . The results for $\lambda/20$ rms height surfaces with power law slopes of -3, -2.5, and -4.5 are compared for a polar angle of 20 degree, cutoff wavenumber $k_c = 4\pi/\lambda$, and dielectric constant of 50 + i30. The results show that the U_B parameter is larger for the -2.5 slope surface, which has more high frequency content and hence larger slopes, and that U_B is smaller for the smoother -4.5 slope surface. However, U_B exists for all three cases and indicates the direction of surface periodicity in each case.

Finally, Figure 6 investigates the effect of the high frequency cutoff wavenumber, k_c , on U_B . Plotted are the results from $\lambda/20$ rms height -3 slope surfaces for a polar angle of 20 degrees and dielectric constant 50 + i30. Cutoff wavenumbers of $4\pi/\lambda$, $8\pi/\lambda$, and $16\pi/\lambda$ are shown. This change in the cutoff wavenumber is seen to have little effect on the U_B results.

5 Conclusions

A numerical study of polarimetric thermal emission from randomly rough ocean surfaces using a Monte Carlo method has been carried out. This study indicates that polarimetric information can be useful in the remote sensing of anisotropic rough ocean surfaces. One proposed application is the remote sensing of wind direction over the ocean, as the rough surface created on the ocean has an anisotropic structure. Since the U_B parameter is shown to be relatively insensitive to the polar angle, the permittivity of the medium, and the cutoff wavenumber of the surface spectral density function as an indicator of surface azimuthal direction, a wind direction sensor could feasibly operate under a wide variety of these conditions. Further research into this area and into the use of a more realistic ocean surface model will continue.

Acknowledgements This work was supported in part by ONR Grant N00014-92-J-1616, NASA grant NAGW-1617, and a National Science Foundation Graduate Research Fellowship.

IV. REFERENCES

- [1] Tsang, L., "Polarimetric passive microwave remote sensing of random discrete scatterers and rough surfaces," *J. Electromag. Waves Applic.*, Vol. 5, No. 1, 41-57, 1991.
- [2] Veysoglu, M. E., H. A. Yueh, R. T. Shin and J. A. Kong, "Polarimetric passive remote sensing of periodic surfaces," *J. Electromag. Waves Applic.*, Vol. 5, No. 3, 267-280, 1991.
- [3] Nghiem, S. V., M. E. Veysoglu, J. A. Kong, R. T. Shin, K. O'Neill, and A. W. Lohanick, "Polarimetric passive remote sensing of a periodic soil surface: microwave measurements and analysis," *J. Electromag. Waves Applic.*, Vol. 5, No. 9, 997-1005, 1991.
- [4] Johnson, J. T., J. A. Kong, R. T. Shin, K. O'Neill, and A. Lohanick, "Third Stokes parameter emission from a periodic water surface.", submitted to *IEEE Trans. Geosci. Remote Sensing*, 1992.
- [5] Yueh, S. H. S. V. Nghiem, R. Kwok, F. K. Li, J. T. Johnson, and J. A. Kong, "Polarimetric thermal emission from periodic water surfaces," submitted to *Radio Science*, 1992.
- [6] Tsang, L., J. A. Kong, and R. T. Shin, *Theory of Microwave Remote Sensing*, John Wiley, New York, 1985.
- [7] Thorsos, E. I., "The validity of the Kirchhoff approximation for rough surface scattering using a Gaussian roughness spectrum," *J. Acoust. Soc. Am.*, Vol. 83, No. 1, 78-92, 1988.
- [8] Fung, A. K. and M. F. Chen, "Numerical simulation of scattering from simple and composite random surfaces," *J. Opt. Soc. Am. A*, Vol. 2, No. 12, 2274-2284, 1985.
- [9] Chuang, S. L. and J. A. Kong, "Wave scattering from a periodic dielectric surface for a general angle of incidence," *Radio Science*, Vol. 17, No. 3, 545-557, 1982.
- [10] Wentz, F. J. "Measurement of oceanic wind vector using satellite radiometers," *IEEE Trans. Geosci. Remote Sens.*, Sept. 1992.

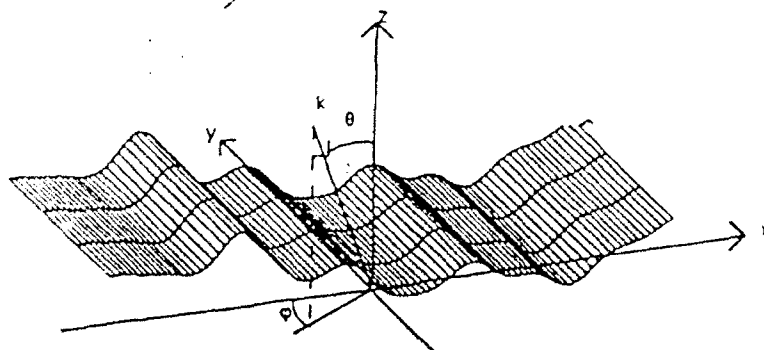


Figure 1: Geometry of the problem

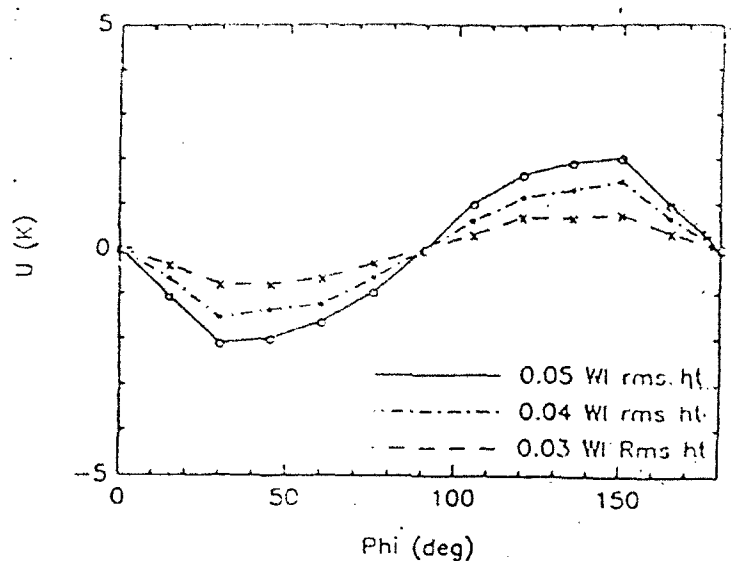


Figure 2: Variation of U_B with rms ht

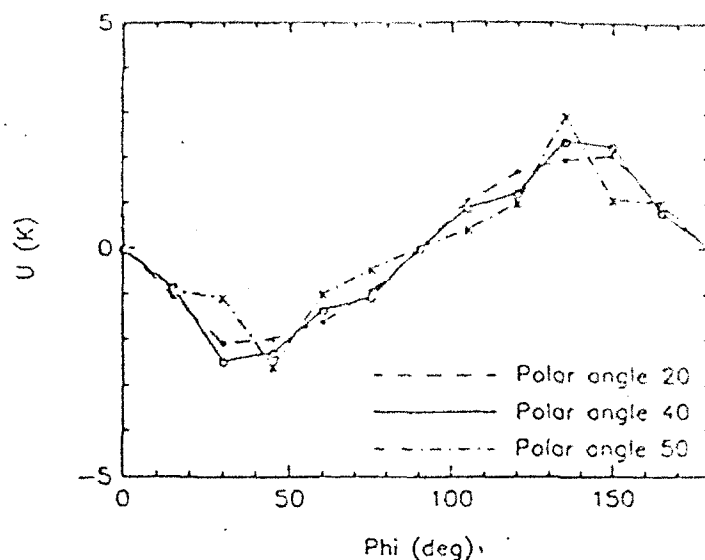


Figure 3: Variation of U_B with polar angle

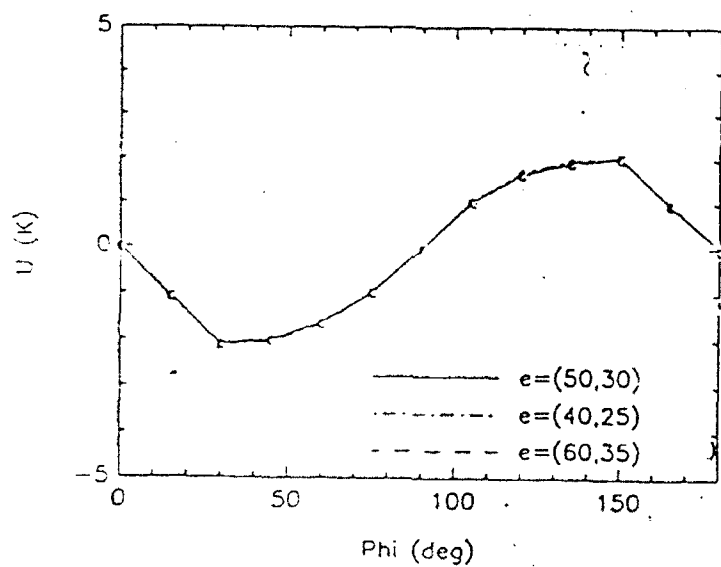


Figure 4: Variation of U_B with surface permittivity

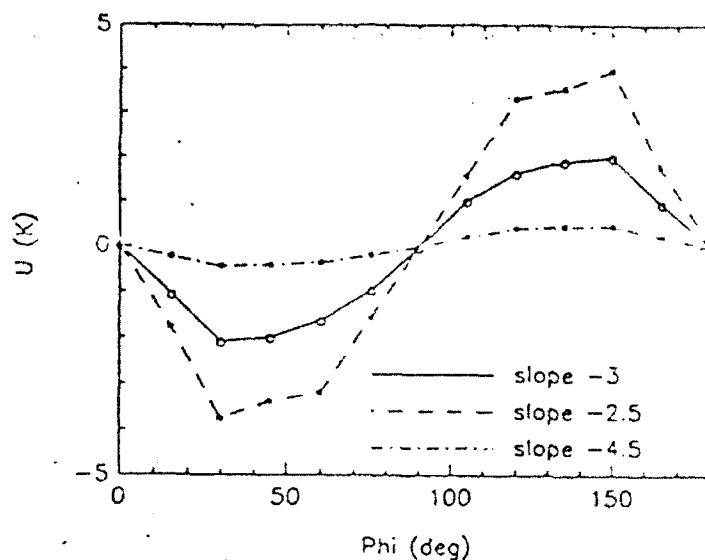


Figure 5: Variation of U_B with power law slope

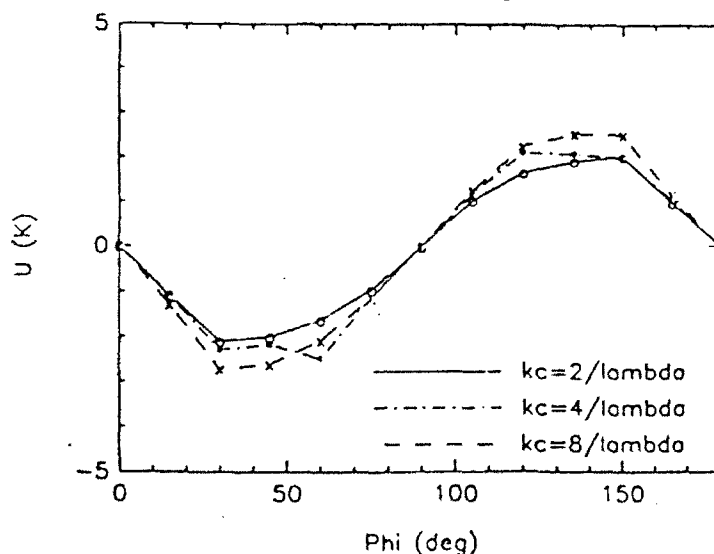


Figure 6: Variation of U_B with high frequency cutoff

Polarimetric Thermal Emission from Rough Ocean Surfaces

J. T. Johnson, J. A. Kong, and R. T. Shin
Department of Electrical Engineering and Computer Science
and Research Laboratory of Electronics
Massachusetts Institute of Technology, Cambridge, MA

S. H. Yueh, S. V. Nghiem, and R. Kwck
Jet Propulsion Laboratory
California Institute of Technology, Pasadena, CA

Short Title: Polarimetric Thermal Emission from Ocean Surfaces

Correspondence should be sent to:

Prof. J. A. Kong
Rm 26-305, MIT
Cambridge, MA 02139

Abstract

A numerical study of the polarimetric thermal emission from ocean surfaces randomly rough in one dimension using a Monte Carlo technique is presented. In this study, a set of finite length surface profiles with desired statistics was generated using a spectral method. Each surface was extended periodically to create an infinite rough surface, and the thermal emission was computed using the extended boundary condition method (EBC) and the method of moments (MOM). The results from the set of surfaces were then averaged to obtain the Monte Carlo estimate of polarimetric thermal emission. The surface statistics chosen were intended to model a wind perturbed ocean surface in the X to K_u band microwave region. The results of the study show that the third Stokes parameter, U_B , is sensitive to the azimuthal angle between the surface periodicity and the looking angle, the rms height of the surface, and the surface power law spectrum slope, and that this parameter is insensitive to variations in polar angle, permittivity, and surface spectrum high frequency content.

1 Introduction

Recent theoretical works have suggested the potential of passive polarimetry in the remote sensing of geophysical media [1-5]. It has been shown that the brightness temperature in the third Stokes parameter, U_B , may become large for azimuthally asymmetric fields of observation. In references [4] and [5], values of U_B as high as 30 K were measured from sinusoidal water surfaces at 10 and 14.6 GHz. In order to investigate the potential applicability of passive polarimetry to the remote sensing of rough ocean surfaces, a numerical study of the polarimetric thermal emission from ocean surfaces randomly rough in one dimension was performed. A Monte Carlo technique utilizing an exact integral equation method for calculating thermal emission was chosen for the study.

The next section presents a brief background on the theory of polarimetry and describes the passive polarimetric brightness vector. The method of calculation for the numerical experiment is discussed in Section 3 and its convergence investigated in Section 4. Finally, the numerical results are presented in Section 5.

2 Theory of Polarimetry

In passive polarimetry, brightness temperatures corresponding to all of the four modified Stokes parameters are measured. The brightness temperature Stokes vector is defined as

$$\bar{T}_B = \frac{1}{C} \bar{I} = \frac{1}{C} \begin{bmatrix} I_h \\ I_v \\ U \\ V \end{bmatrix} = \frac{1}{\eta C} \begin{bmatrix} \langle E_h E_h^* \rangle \\ \langle E_v E_v^* \rangle \\ 2\text{Re}\langle E_v E_h^* \rangle \\ 2\text{Im}\langle E_v E_h^* \rangle \end{bmatrix} \quad (1)$$

where E_h and E_v are the emitted electric fields received from the horizontally and vertically polarized channels of the radiometer, η is the characteristic impedance, and $C = K/\lambda^2$ with K denoting Boltzmann's constant, λ the wavelength. The first two parameters of the brightness temperature Stokes vector correspond to the received powers in the horizontally and vertically polarized channels, respectively. The third and fourth parameters correspond to the complex correlation between the electric fields received by the horizontally and vertically polarized channels. We will label the four parameters T_{Bh} , T_{Bv} , U_B , and V_B respectively in this paper. It is shown in [3] that the third and fourth Stokes parameters may be related to the brightness temperature in a 45 degree linearly polarized measurement

(T_{Bl}) and a right hand circularly polarized measurement (T_{Br}) as follows:

$$U_B = 2T_{Bl} - T_{Bh} - T_{Bv} \quad (2)$$

$$V_B = 2T_{Br} - T_{Bh} - T_{Bv} \quad (3)$$

Thus, to calculate all four parameters of the brightness temperature Stokes vector, the brightness temperatures in horizontal, vertical, 45 degree linear, and right hand circular polarizations are first calculated, and the above equations are used to obtain U_B and V_B .

In the passive remote sensing of rough surfaces, the parameter that is actually of interest is the emissivity, which relates the brightness temperature emitted by an object to its actual physical temperature, under the assumption that the object is at a constant physical temperature and that the emission from the object is the only source of brightness:

$$T_{Ba} = e_a(\theta, \phi) T_{phys} \quad (4)$$

In the above equation, the subscript a refers to the polarization of the brightness temperature, θ to the polar observation angle, and ϕ to the azimuthal observation angle. Through the principles of energy conservation and reciprocity, Kirchhoff's law relates this emissivity to the reflectivity of the surface [6]:

$$e_a(\theta, \phi) = 1 - r_a(\theta, \phi) \quad (5)$$

The reflectivity $r_a(\theta, \phi)$ for the given incident polarization a is defined as the fraction of the power incident from direction (θ, ϕ) that is rescattered and can be evaluated by integrating the bistatic scattering coefficient $\gamma_{ba}(\theta, \phi; \theta', \phi')$ over all scattering angles in the upper hemisphere and summing the results of both orthogonal scattering polarizations.

$$r_a(\theta, \phi) = \frac{1}{4\pi} \sum_b \int_0^{\pi/2} d\theta' \sin \theta' \int_0^{2\pi} d\phi' \gamma_{ba}(\theta, \phi; \theta', \phi') \quad (6)$$

In the above expression, (θ, ϕ) and (θ', ϕ') represent the incident and the scattered directions, respectively, and the subscripts a and b represent the polarizations of the incident and the scattered waves, respectively.

Thus, to calculate the fully polarimetric emission vector, the bistatic scattering coefficient for each of four polarizations is first calculated and integrated over the upper hemisphere to obtain the reflectivity for that particular polarization. Multiplication of the corresponding emissivity by the physical temperature of the object under view yields the

brightness temperature for this polarization. The fully polarimetric brightness vector is then calculated as described previously. A physical temperature of 300 K was assumed for the surfaces in this experiment.

3 Method of Calculation

Scattering from randomly rough surfaces has been studied extensively by a number of researchers. Numerous approximate techniques, such as the Kirchhoff approximation and the small perturbation method, exist and work well under certain restrictions for providing the statistically expected values of scattered fields and power [6]. However, it was found in [2] that in order to measure large U_B values from a sinusoidal surface, a large height to period ratio was required. The large slopes of such a surface fall into the regions of non-applicability for the above methods, so a Monte Carlo method was chosen for the study.

In this Monte Carlo method, a set of surface profiles with given statistics was generated, and the fully polarimetric brightness vector from each surface was calculated using an exact integral equation approach. The results for the set were then averaged to obtain the final Monte Carlo estimate of the average brightness vector for those particular surface parameters. The surface generation and analysis procedure are described in more detail in the next section.

3.1 Random surface generation

A spectral method, described in [7-8], was used to generate a finite sample of a rough surface with desired statistics. In this method, a set of normally distributed (both real and imaginary part) Fourier coefficients is generated and then weighted by a spectral density function in the frequency domain. This spectral density function corresponds to the desired spectral density of the surface set; it is also the Fourier transform of the desired correlation function for the set. The resulting Fourier coefficients are then transformed back into the space domain using an inverse FFT algorithm to obtain a surface profile sampled in space. The surface profiles were linearly interpolated between the specified points.

Since only a finite surface profile could be generated, an infinite surface was created by extending this finite surface periodically. The Floquet modes obtained from the periodic surface are thus a discrete approximation to the continuous spectrum of a truly infinite

random rough surface. The effect of this periodic extension on the polarimetric brightness temperature was investigated by comparing the results from a set of surfaces with a given period with the results from a set of surfaces with twice that period and the same frequency spectrum. A period of 20λ was found to be sufficient to provide convergence of the results for longer period surfaces, as will be discussed in Section 4. The surface was continuous when made periodic due to the periodic properties of the FFT series from which it was generated.

The surface profiles generated were rough in one direction only due to the complexity of the calculations for surfaces rough in two spatial directions. The rough profile along the x direction was extended infinitely along the y direction in the calculations (see Figure 1). Three dimensional angles of incidence were allowed, however, so that polarimetric effects could be observed from the resulting 'conical diffraction' problem. While this model is extremely simple when compared to an actual wind perturbed ocean surface, its results should give some indication as to the properties of U_B for general rough surfaces.

The surface statistics chosen for the calculations were intended to model ocean surfaces in the microwave frequency range. For this purpose, a dielectric constant of $50 + i30$ was chosen for the medium and a power-law spectral density function for the surfaces was used. This function, $\phi(k)$ is described by:

$$\phi(k) = \begin{cases} k^{-s} & 2\pi/5\lambda \leq k \leq k_c \\ 0 & \text{otherwise} \end{cases} \quad (7)$$

where k is the spatial wavenumber of the surface in rads/m , s is the slope of the power law spectrum, and k_c is the cutoff wavenumber of the surface set. The effects of varying the slope of the spectrum and its cutoff were investigated in the experiment. The surface in Figure 1 is one of the generated $s = 3$ slope power law spectra surfaces with a high frequency cutoff of $k_c = 4\pi/\lambda$ and period of 5λ .

Each surface was normalized independently of the others to a specified rms surface height; rms heights of 0.075λ , 0.05λ , 0.033λ were chosen to investigate the effect of varying the surface height on the polarimetric brightness temperature. The 20λ requirement for the surface period prevents larger rms heights from being studied due to computational limitations. Each generated surface consisted of 400 points within this period, so that the surface profile was sampled every $\lambda/20$ along the \hat{x} direction. This sampling frequency is well above all of the Nyquist frequencies of the power spectral density functions used in the experiment. The surface statistics calculated from the generated surface sets were

compared to their desired theoretical values and found to be in good agreement.

The results from twenty surface profiles were averaged for all of the 0.075λ rms height points in the experiment. The convergence of the results with the number of surface profiles averaged was investigated by comparing the results from independent groups of twenty surfaces for one case of the experiment. The results for U_B were found to be within 0.5 K for the 0.075λ rms height surfaces at polar angle 20 degrees, as is discussed in Section 4.

3.2 Integral Equation Method

Numerous studies have been made of scattering from a periodic surface. The Extended Boundary Condition (EBC) method [9] is one of the most efficient methods, but has been found to become ill conditioned for steep surfaces. The Method of Moments (MOM) for a periodic surface, described in [2], is another solution of the problem that does not have the steep surface problems of the EBC, but is more computationally intensive. The calculations from these two methods were compared for a sample surface for each case in the experiment and found to give similar results in all of the cases. This agreement indicates that the surface slope limitations of the EBC were not exceeded, and this more efficient method of calculation was used for the larger surface sets of the experiment.

4 Verification of Convergence

Two convergence issues are important for this Monte Carlo method: the convergence of the results with the number of surfaces averaged and the convergence of the results with the period of the surfaces analyzed. Both issues are investigated in this section.

The convergence of the results with the number of surfaces averaged is the first type of convergence that must be investigated. To check this type, independent groups of surfaces were analyzed and their results compared. It was found that the difference obtained in the average U_B values from ten surface profiles were within 0.3 K for all of the cases with rms height less than or equal to 0.05λ . For the rms height 0.075λ case, twenty surface profiles were averaged, and a maximum U_B difference of 0.5 K in the average from independent sets of twenty surfaces was observed. Since this uncertainty is much less than the azimuthal variation of U_B obtained in the study, these averages were considered sufficient for the study.

The second type of convergence, convergence with respect to the period of the surfaces analyzed, was also investigated. This convergence was verified by comparing the average results from groups of ten surfaces which had different periods but the same frequency spectra. In effect, this procedure corresponds to sampling the frequency spectrum at a greater number of points in the frequency domain as the period is allowed to increase. Longer scale variations were cutoff as the period was increased. Figure 2 displays the change in polarimetric brightness temperature as the period was increased for 0.05λ rms height surfaces at a polar angle of 20 degrees with power law slope $s = 3$ and cutoff wavenumber $4\pi/\lambda$. Plotted are the results for surfaces with periods of 5λ , 10λ , 15λ , 20λ , and 25λ .

The characteristic "jumps" of periodic surface scattering are observed in all of these curves, but it is seen that the effect becomes less pronounced as the period is increased. This is due to the fact that a greater number of Floquet modes is obtained for the longer period surfaces, which results in a smaller shift in total power as one mode makes the transition from propagating to non-propagating. Figure 3 compares the results for the 20λ and 25λ period surfaces alone. It is seen that these curves are fairly smooth in azimuthal angle and that they agree to within 0.2 K in U_B for all of the angles analyzed. The results from period 20λ and 25λ surfaces were also compared for a set of twenty rms height 0.075λ surfaces. For this case, a maximum difference of 1.5 K was obtained in the U_B results. However, the U_B results are also larger for this case, so that the uncertainty is approximately the same percentage of U_B as in the smaller rms height cases. A period of 20λ was chosen for all of the surfaces throughout the rest of the experiment.

5 Results of calculations

Figure 4 is a plot of the average U_B value for the 0.075λ , 0.05λ , and 0.033λ rms height surfaces as a function of azimuthal angle for a polar angle of 20 degrees. A power law slope of $s = 3$, cutoff wavenumber of $k_c = 4\pi/\lambda$, and dielectric constant of $50 + i30$ were used in the calculations. Points were calculated every 15 degrees in azimuthal angle, so that the interpolating lines shown should not be taken to be exact. It is seen that the U_B value is small for viewing angles parallel or perpendicular to the direction of periodicity of the surface, and that the highest values of U_B are obtained at azimuthal angles of approximately 45 or 135 degrees. The magnitude of U_B is determined by the rms height of

the surface, with rougher surfaces giving higher values. The small values of U_B obtained in these results (5 K) are due to the convergence requirements for the Monte Carlo technique: larger U_B values could be obtained by analyzing rougher surfaces, but would require more computer time than was available for this study. Also, data collected from the SSM/I and reported by Wentz [10] indicates that the azimuthal variation in T_{Bh} and T_{Bv} for real wind perturbed ocean surfaces at both 37 and 19 GHz is typically less than 3 K, as is obtained for these rms heights. The U_B channel is seen to indicate the azimuthal direction of the surface in all cases where it is observable. Note that negative values for U_B are possible, as this parameter corresponds only to a correlation between real observables. Also, the symmetry about $\phi = 90$ deg seen in Figure 2 and the following figures is due only to the statistical symmetry of the surface set about this angle; individual surfaces are not symmetric about $\phi = 90$ deg. This gives an indication that the average of the surface profiles is converging to the true statistical average.

Figure 5 investigates the effects of polar angle on the U_B . Plotted are the results at polar angles of 20, 40, and 50 degrees for the 0.075λ rms height, $s = 3$, $k_c = 4\pi/\lambda$, $50 + i30$ dielectric constant surfaces. The results are surprisingly similar, demonstrating that this parameter is relatively insensitive to polar angle as an indicator of surface azimuthal direction. These larger polar angles are important due to the need for large polar angles in satellite borne sensor applications.

Figure 6 illustrates the effect of permittivity on U_B . Results for polar angle 20 degrees, rms height 0.075λ , $s = 3$, $k_c = 4\pi/\lambda$, and dielectric constants of $40 + i25$, $50 + i30$, and $60 + i35$ are plotted. The results again indicate that the U_B channel is insensitive to a change in the dielectric constant around $50 + i30$.

Figure 7 displays the variation in U_B with the slope of the power law spectrum, s . The results for 0.075λ rms height surfaces with power law slopes of $s = 3$, $s = 2.5$, and $s = 3.5$ are compared for a polar angle of 20 degree, cutoff wavenumber $k_c = 4\pi/\lambda$, and dielectric constant of $50 + i30$. The results show that the U_B parameter is larger for the $s = 2.5$ surface, which has more high frequency content and hence larger slopes, and that U_B is smaller for the smoother $s = 3.5$ slope surface. However, U_B exists for all three cases and indicates the direction of surface periodicity in each case.

Finally, Figure 8 investigates the effect of the high frequency cutoff wavenumber, k_c on U_B . Plotted are the results from 0.075λ rms height $s = 3$ surfaces for a polar angle of 20 degrees and dielectric constant $50 + i30$. Cutoff wavenumbers of $4\pi/\lambda$, $8\pi/\lambda$, and $16\pi/\lambda$

are shown. This change in the cutoff wavenumber is seen to have little effect on the U_B results.

6 Conclusions

A numerical study of polarimetric thermal emission from randomly rough ocean surfaces using a Monte Carlo method has been carried out. This study indicates that polarimetric information can be useful in the remote sensing of anisotropic rough ocean surfaces. One proposed application is the remote sensing of wind direction over the ocean, as the rough surface created on the ocean has an anisotropic structure. Since the U_B parameter is shown to be relatively insensitive to the polar angle, the permittivity of the medium, and the cutoff wavenumber of the surface spectral density function, a wind direction sensor could feasibly operate under a wide variety of these conditions. Further research into the area and into the use of a more realistic ocean surface model will continue.

Acknowledgements This work was supported in part by ONR grant N00014-92-J-1616, NASA grant NAGW-1617, and a National Science Foundation Graduate Research Fellowship.

7 References

- [1] Tsang, L., "Polarimetric passive microwave remote sensing of random discrete scatterers and rough surfaces," *J. Electromag. Waves Applic.*, Vol. 5, No. 1, 41-57, 1991.
- [2] Veysoglu, M. E., H. A. Yueh, R. T. Shin and J. A. Kong, "Polarimetric passive remote sensing of periodic surfaces," *J. Electromag. Waves Applic.*, Vol. 5, No. 3, 267-280, 1991.
- [3] Nghiem, S. V., M. E. Veysoglu, J. A. Kong, R. T. Shin, K. O'Neill, and A. W. Lohanick, "Polarimetric passive remote sensing of a periodic soil surface: microwave measurements and analysis," *J. Electromag. Waves Applic.*, Vol. 5, No. 9, 997-1005, 1991.
- [4] Johnson, J. T., J. A. Kong, R. T. Shin, K. O'Neill, and A. Lohanick, "Third Stokes parameter emission from a periodic water surface," submitted to *IEEE Trans. Geosci. Remote Sensing*, 1992.
- [5] Yueh, S. H. S. V. Nghiem, R. Kwok, F. K. Li, J. T. Johnson, and J. A. Kong, "Polarimetric thermal emission from periodic water surfaces," submitted to *Radio Science*, 1992.
- [6] Tsang, L., J. A. Kong, and R. T. Shin, *Theory of Microwave Remote Sensing*, John Wiley, New York, 1985.
- [7] Thorsos, E. I., "The validity of the Kirchhoff approximation for rough surface scattering using a Gaussian roughness spectrum," *J. Acoust. Soc. Am.*, Vol. 83, No. 1, 78-92, 1988.
- [8] Fung, A. K. and M. F. Chen, "Numerical simulation of scattering from simple and composite random surfaces," *J. Opt. Soc. Am. A*, Vol. 2, No. 12, 2274-2284, 1985.
- [9] Chuang, S. L. and J. A. Kong, "Wave scattering from a periodic dielectric surface for a general angle of incidence," *Radio Science*, Vol. 17, No. 3, 545-557, 1982.
- [10] Wentz, F. J. "Measurement of oceanic wind vector using satellite radiometers," *IEEE Trans. Geosci. Remote Sens.*, Sept. 1992.

Figure 1: Geometry of the problem

Figure 2: Convergence of polarimetric brightness temperature with period of surfaces (a) U_B (b) T_{Bh} (c) T_{Bv} (d) V_B

Figure 3: Comparison of average brightness temperatures for 20λ and 25λ period surfaces (a) U_B (b) T_{Bh} (c) T_{Bv} (d) V_B

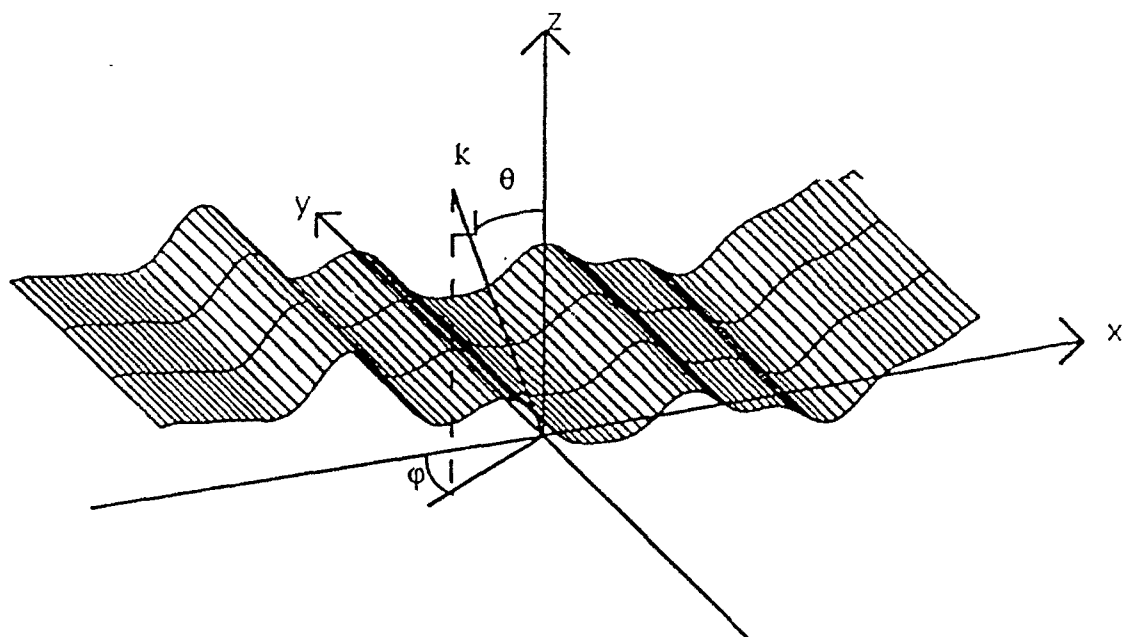
Figure 4: Effect of rms height on polarimetric brightness temperature (a) U_B (b) T_{Bh} (c) T_{Bv} (d) V_B

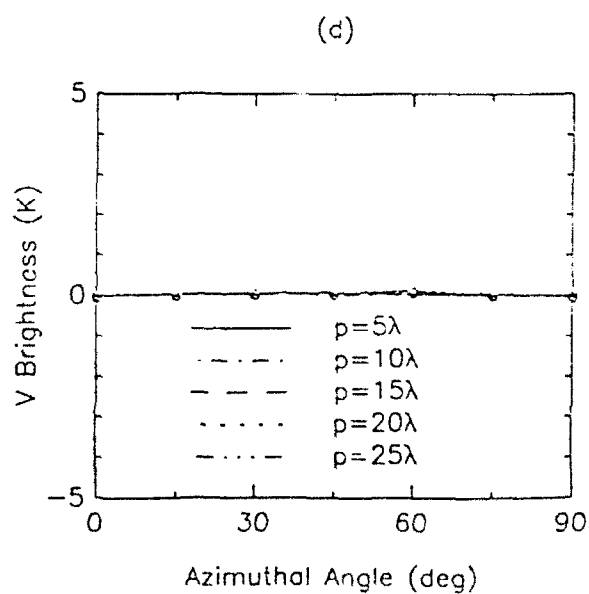
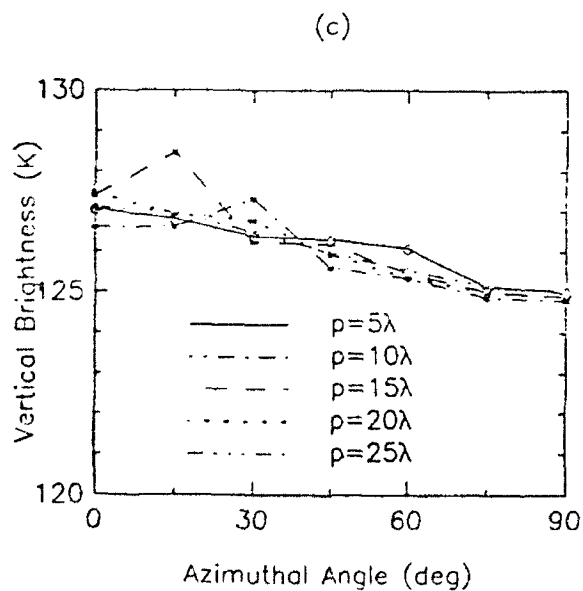
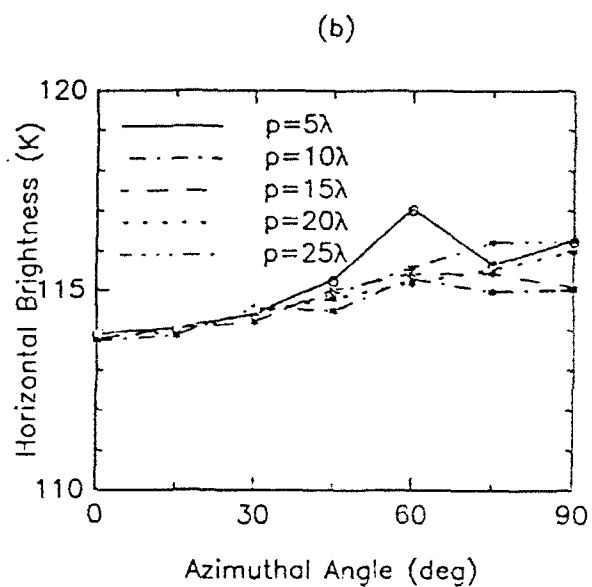
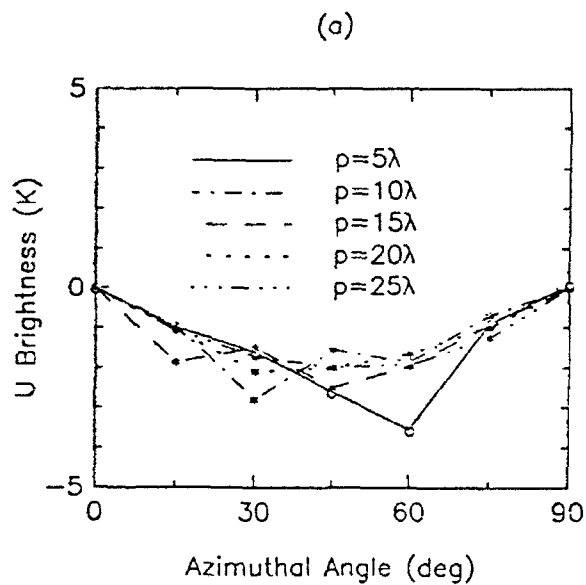
Figure 5: Effect of polar angle on polarimetric brightness temperature (a) U_B (b) T_{Bh} (c) T_{Bv} (d) V_B

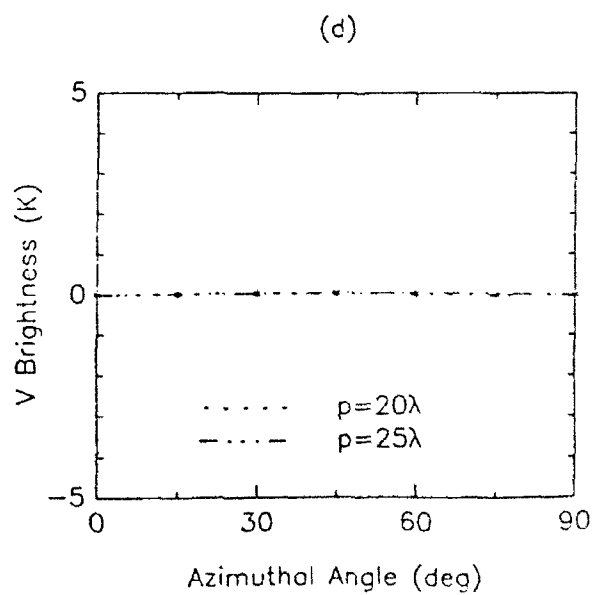
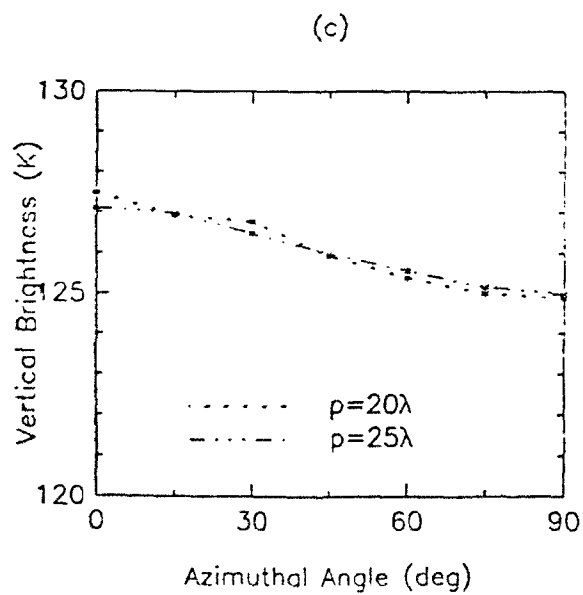
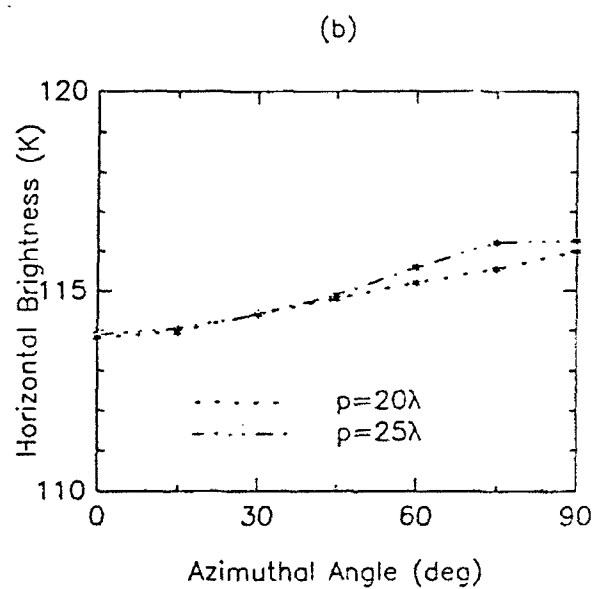
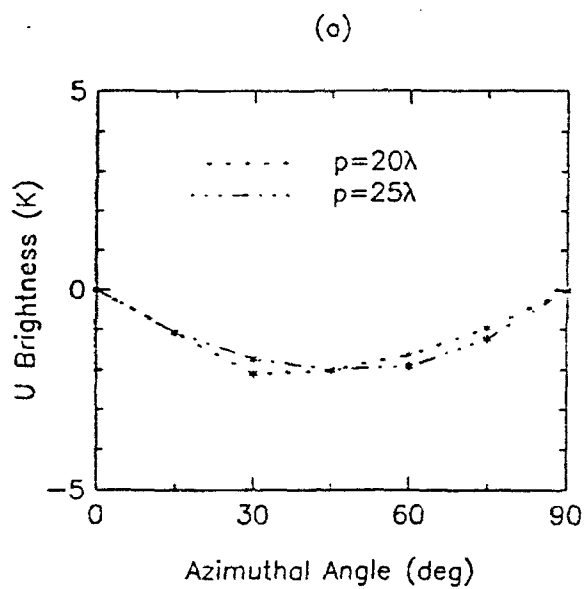
Figure 6: Effect of permittivity on polarimetric brightness temperature (a) U_B (b) T_{Bh} (c) T_{Bv} (d) V_B

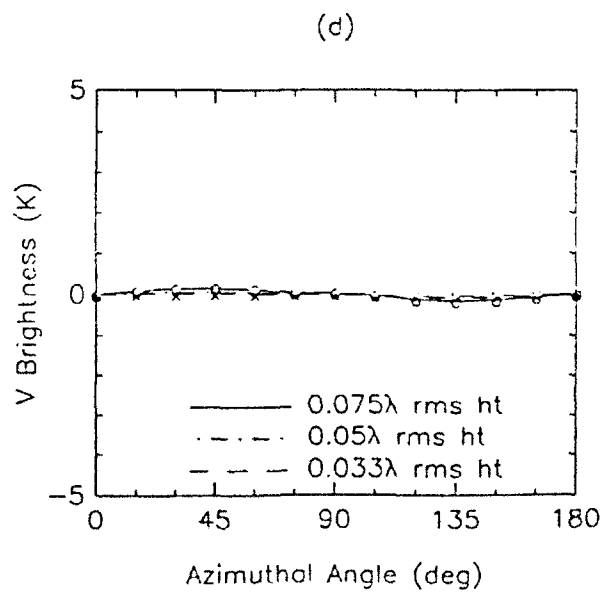
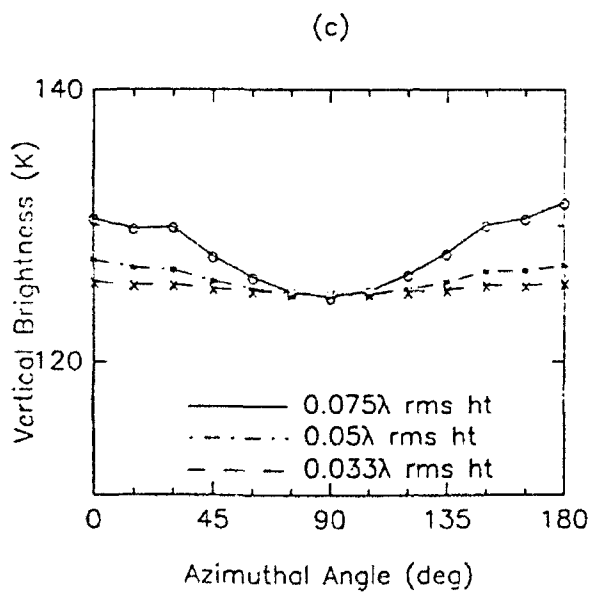
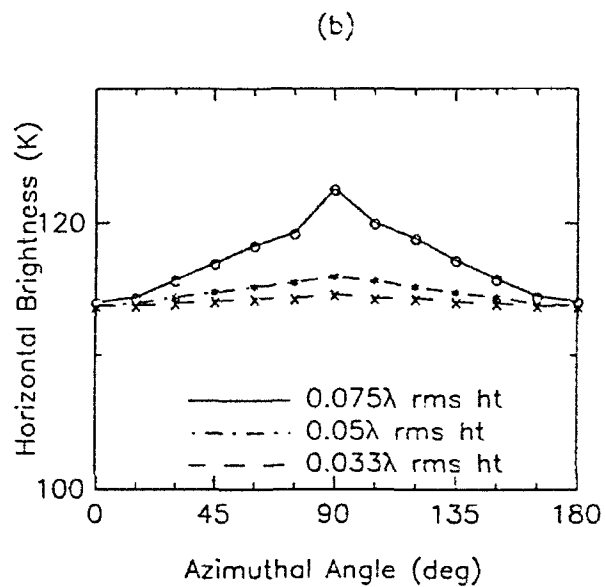
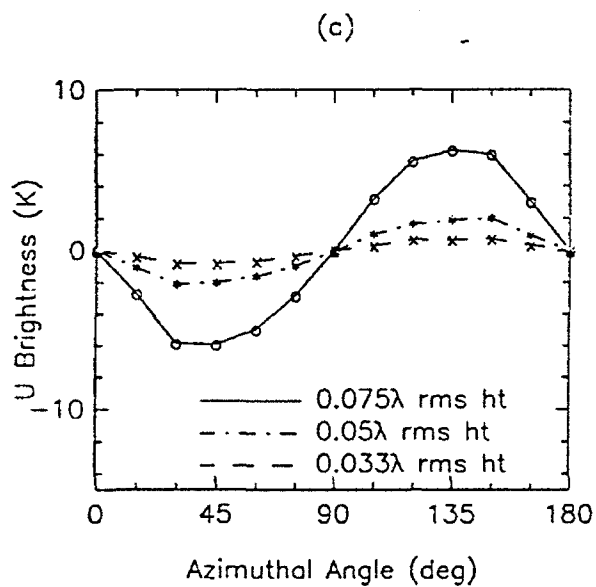
Figure 7: Effect of power law slope on polarimetric brightness temperature (a) U_B (b) T_{Bh} (c) T_{Bv} (d) V_B

Figure 8: Effect of cutoff wavenumber on polarimetric brightness temperature (a) U_B (b) T_{Bh} (c) T_{Bv} (d) V_B

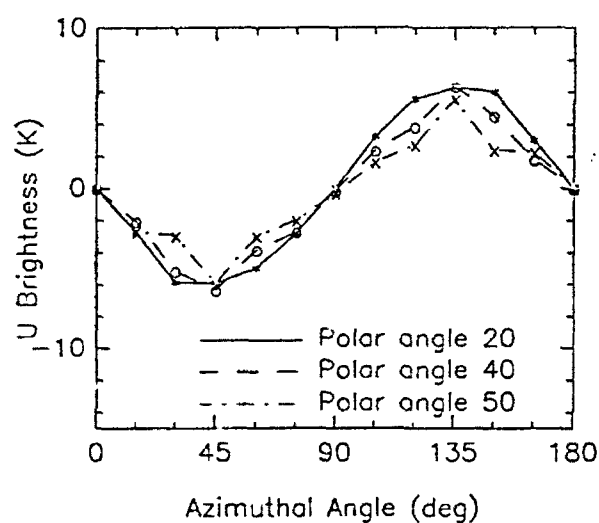




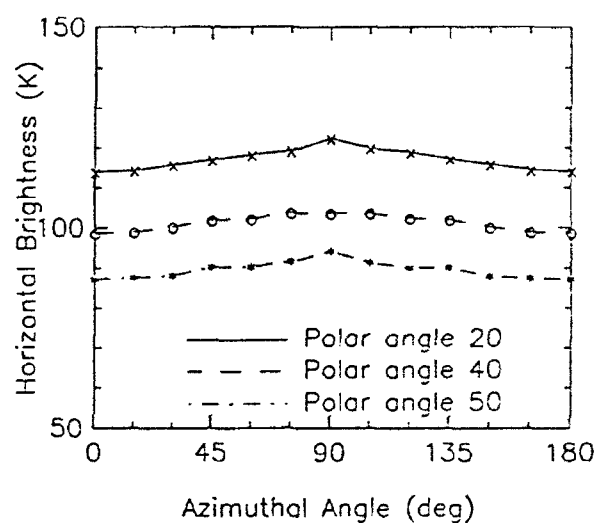




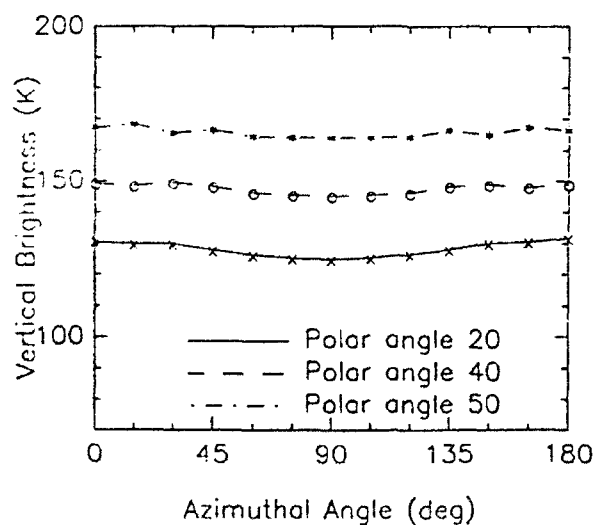
(a)



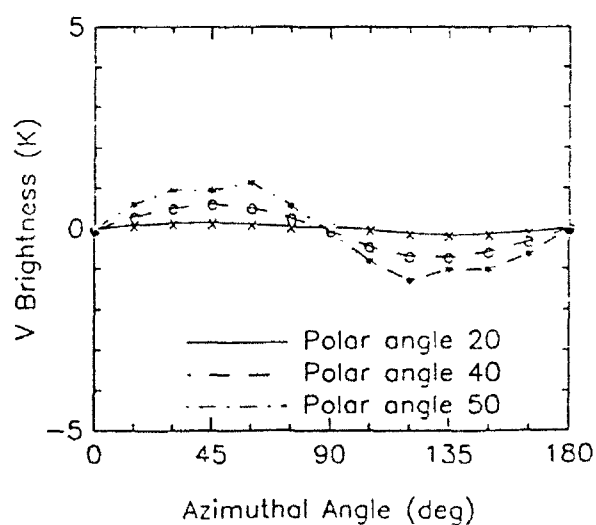
(b)

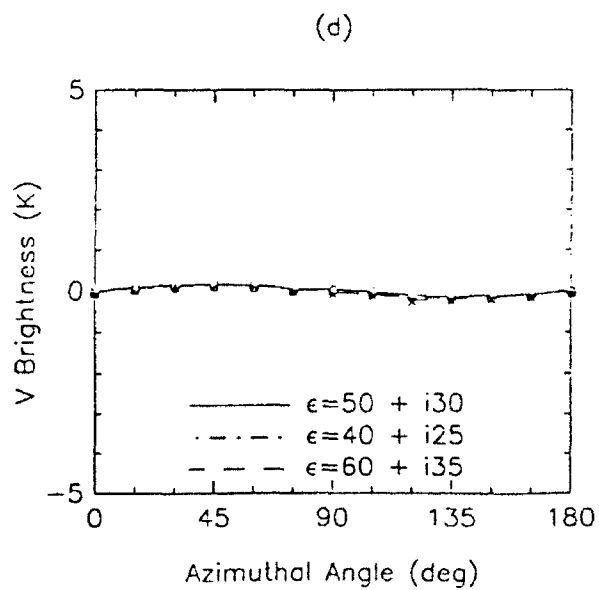
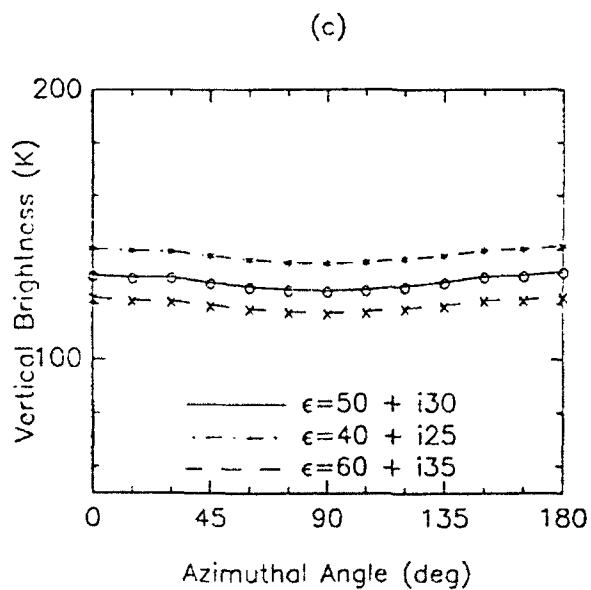
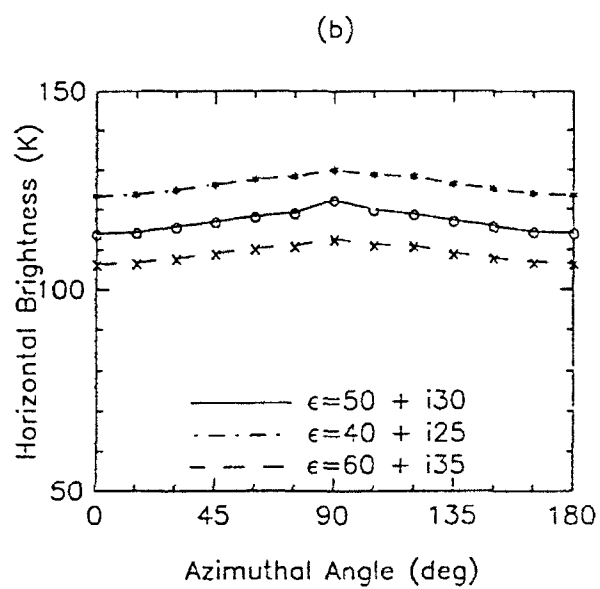
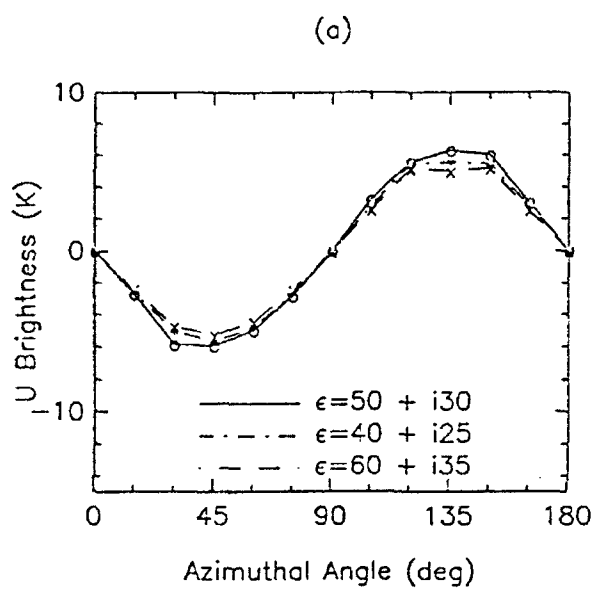


(c)

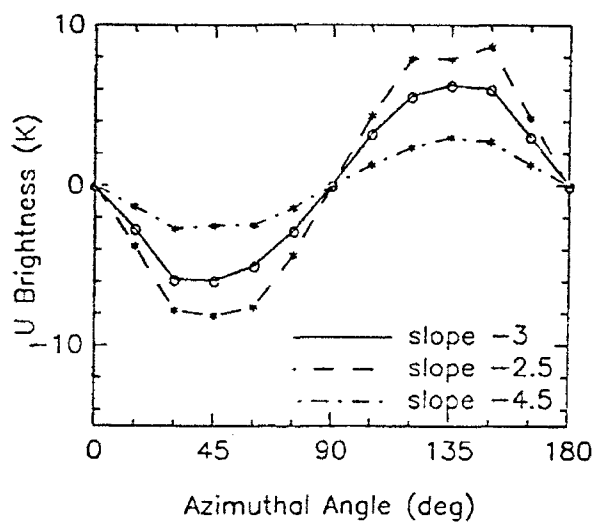


(d)

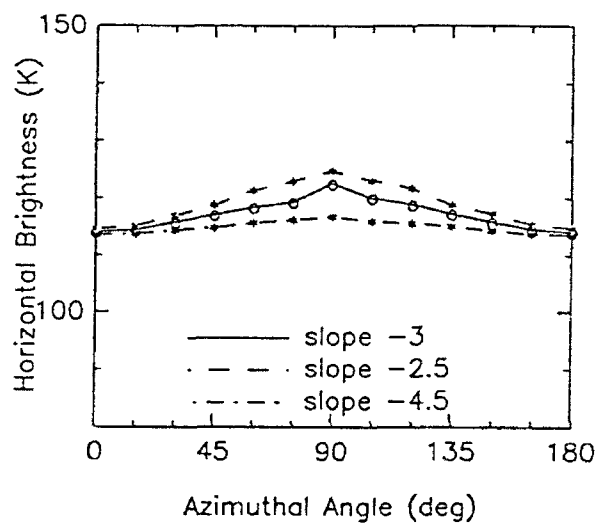




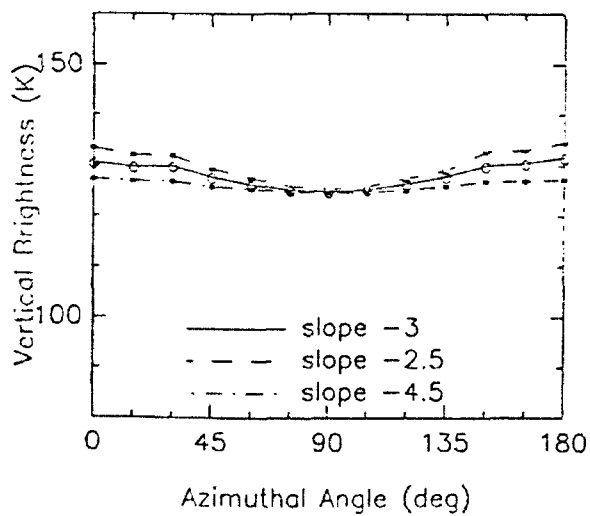
(a)



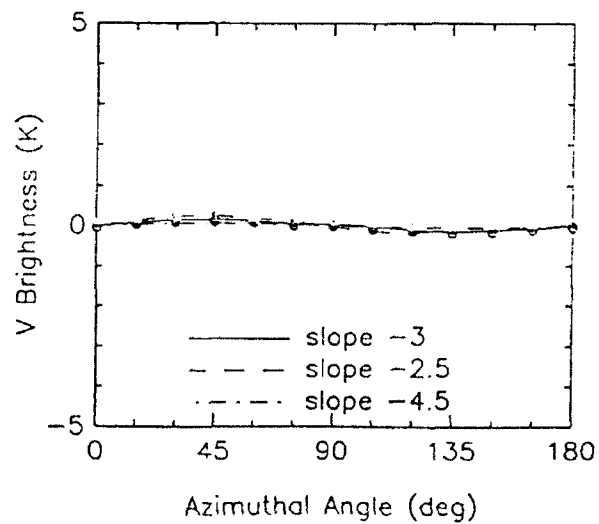
(b)

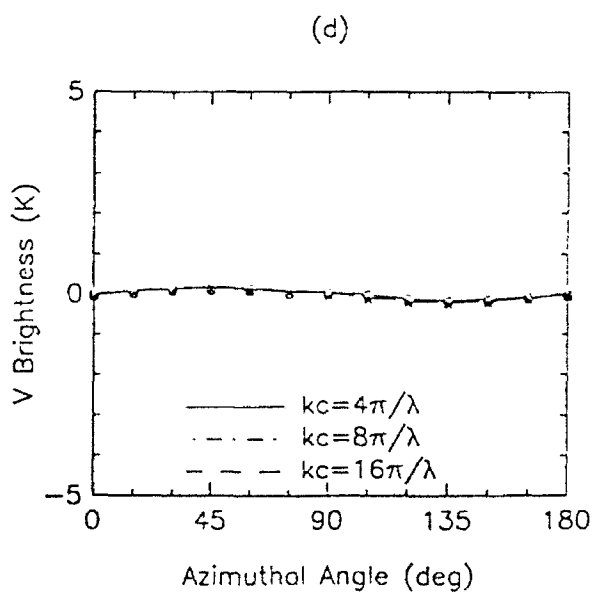
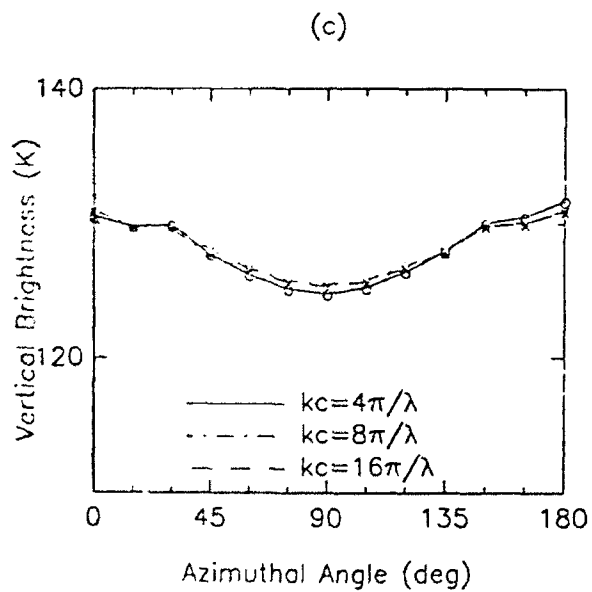
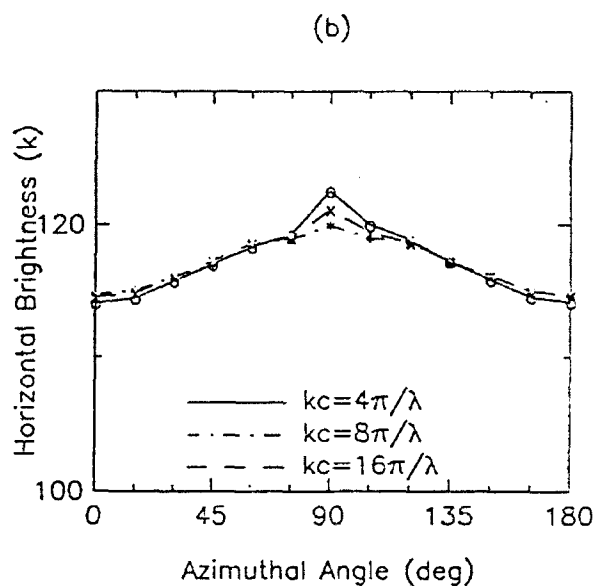
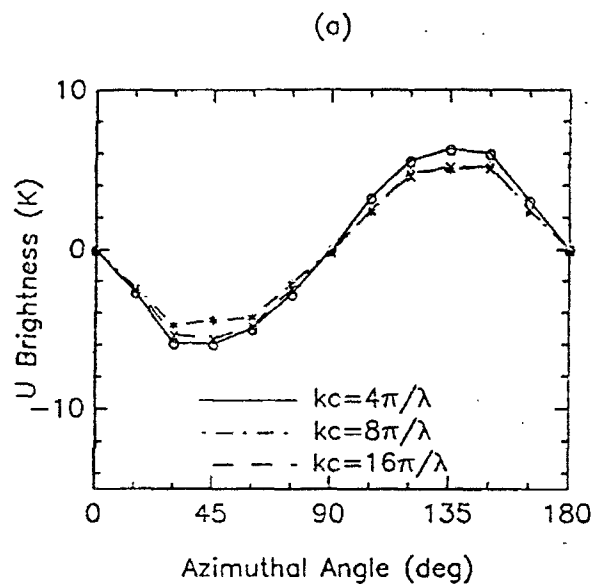


(c)



(d)





Third Stokes Parameter Emission from a Periodic Water Surface

J. T. Johnson, J. A. Kong, R. T. Shin, and D. H. Staelin
Department of Electrical Engineering and Computer Science
and Research Laboratory of Electronics
Massachusetts Institute of Technology, Cambridge, MA

K. O'Neill and A. Lohanick
Cold Regions Research and Engineering Laboratory, Hanover, NH

Abstract An experiment in which the third Stokes parameter thermal emission from a periodic water surface was measured is documented. This parameter is shown to be related to the direction of periodicity of the periodic surface and to approach brightnesses of up to 30 K at X band for the surface used in the experiment. The surface actually analyzed was a "two-layer" periodic surface; the theory of thermal emission from such a surface is derived and the theoretical results are found to be in good agreement with the experimental measurements. These results further the idea of using the third Stokes parameter emission as an indicator of wind direction over the ocean.

1 Introduction

Recent theoretical works have suggested the potential of passive polarimetry in the remote sensing of geophysical media [1-3]. These works indicate that the third Stokes parameter, U_B , of the thermal emission may become large for azimuthally asymmetric fields of observation. In [3], values of U_B as high as 40 K were measured from a periodic triangular soil surface at 10 GHz, and the U_B parameter was found to indicate the azimuthal angle between the observation angle and the direction of surface periodicity. It has thus been proposed that these properties could make passive polarimetric measurements useful in the remote sensing of wind direction over the ocean, since a wind generated ocean surface has an anisotropic structure. In order to demonstrate the existence of the U_B parameter for a water surface, and thus to investigate the potential applicability of passive polarimetry

to ocean remote sensing, observations of a periodic water surface were performed at the Cold Regions Research and Engineering Laboratory (CRREL), Hanover, NH in September of 1992. This paper documents those observations and the theory developed for the "two-layer" periodic surface actually analyzed in the experiment.

2 Theory of Polarimetry

In passive polarimetry, brightness temperatures corresponding to all four modified Stokes parameters are measured. The brightness temperature Stokes vector is defined as

$$\bar{T}_B = \frac{1}{C} \bar{I} = \frac{1}{C} \begin{bmatrix} I_h \\ I_v \\ U \\ V \end{bmatrix} = \frac{1}{\eta C} \begin{bmatrix} \langle E_h E_h^* \rangle \\ \langle E_v E_v^* \rangle \\ 2\text{Re}\langle E_v E_h^* \rangle \\ 2\text{Im}\langle E_v E_h^* \rangle \end{bmatrix} \quad (1)$$

In the above equation, E_h and E_v are the emitted electric fields received from the horizontal and vertical polarization channels of the radiometer, η is the characteristic impedance, and $C = K/\lambda^2$ with K denoting Boltzmann's constant, λ the wavelength. The first two parameters of the brightness temperature Stokes vector correspond to the received powers for horizontal and vertical polarizations, respectively. The third and fourth parameters correspond to the complex correlation between the electric fields received by the horizontal and vertical channels. We label the four parameters T_{Bh} , T_{Bv} , U_B , and V_B respectively in this paper.

It is shown in [2] that the third and fourth Stokes parameters may be related to the brightness temperature in a 45 degree linearly polarized measurement (T_{Bp}) and a right-hand-circularly polarized measurement (T_{Br}) as follows:

$$U_B = 2T_{Bp} - T_{Bh} - T_{Bv} \quad (2)$$

$$V_B = 2T_{Br} - T_{Bh} - T_{Bv} \quad (3)$$

Thus, to measure all four parameters of the Stokes vector, the brightness temperatures in horizontal, vertical, 45 degree linear, and right-hand-circular polarizations are first measured, and the above equations are used to obtain U_B and V_B .

In the passive remote sensing of rough surfaces, the parameter that is actually of interest is the emissivity, which relates the brightness temperature emitted by an object to its actual physical temperature, under the assumption that the object is at a constant physical temperature, T_{phys} , and that the emission from the object is the only source of brightness:

$$T_{Ba} = e_a(\theta, \phi) T_{phys} \quad (4)$$

In the above equation, the subscript a refers to the polarization of the brightness temperature, θ to the polar observation angle, and ϕ to the azimuthal observation angle. Through the principles of energy conservation and reciprocity, Kirchhoff's Law relates this emissivity to the reflectivity of the surface [4]:

$$e_a(\theta, \phi) = 1 - r_a(\theta, \phi) \quad (5)$$

The reflectivity $r_a(\theta, \phi)$ for the given incident polarization a is defined as the fraction of the power incident from direction (θ, ϕ) that is rescattered and can be evaluated by integrating the bistatic scattering coefficients $\gamma_{ba}(\theta, \phi; \theta', \phi')$ over all scattering angles in the upper hemisphere and summing the results of both orthogonal scattering polarizations:

$$r_a(\theta, \phi) = \frac{1}{4\pi} \sum_b \int_0^{\pi/2} d\theta' \sin \theta' \int_0^{2\pi} d\phi' \gamma_{ba}(\theta, \phi; \theta', \phi') \quad (6)$$

In the expression of the bistatic scattering coefficient, (θ, ϕ) and (θ', ϕ') represent the incident and the scattered directions, respectively, and the subscripts a and b represent the polarizations of the incident and the scattered waves, respectively.

Thus, to calculate the fully polarimetric emission vector, the bistatic scattering coefficient for each of four polarizations is first calculated and integrated over the upper hemisphere to obtain the reflectivity for that particular polarization. Multiplication of the corresponding emissivity by the physical temperature of the object under view yields the brightness temperature for this polarization. The fully polarimetric brightness vector is then calculated as described previously.

3 Two-Layer Periodic Surface Theory

In order to form a periodic water surface, a thin corrugated sheet of fiberglass was placed on top of a flat water surface. After air bubbles trapped underneath were removed, a "two-layer" periodic surface resulted, as shown in Figure 1. In this figure, region zero is the free space region above the periodic surface, with permittivity ϵ_0 and permeability μ_0 , region one is the fiberglass layer, with permittivity ϵ_1 and permeability μ_1 , and region two is the water, with permittivity ϵ_2 and permeability μ_2 . To examine the effects of the fiberglass layer on the measured brightness temperatures, a theoretical model for thermal emission from a two-layer periodic surface was derived and implemented.

The problem of calculating thermal emission from a "single-layer" periodic surface has been solved by several researchers using many different techniques. Two of the methods used in the single-layer case are extended for the two-layer case in this analysis. The results from these two 'exact' methods are then compared to determine which would apply best to the cases measured in the experiment. For both of these methods, the calculations are performed to determine the total power reflected in the reciprocal active problem; this total reflectivity is then used to obtain the emissivity as described previously.

The extended boundary condition (EBC) method described by Chuang and Kong [5] for calculating scattering from a single-layer periodic surface is the first method to be applied. In this method, Huygens' principle is applied at the surface so that the scattered field can be obtained once the surface fields are known. The Huygens' integral equation is solved by expanding the unknown surface fields into Fourier series and forming a truncated impedance matrix which is inverted to obtain the surface fields. This method is known as the extended boundary condition method because the calculations enforce the requirement that the Huygens' integral which equals the field value within the region of interest must be zero outside that region. Although the extended boundary condition method is exact, the numerical formulation becomes ill conditioned if the surface height-to-period ratio becomes too large [10].

To overcome this problem, a second method, the method of moments [9], can be used to perform the calculations. In this formulation, the same Huygens' principle equation is used, but the requirement that the Huygens' integral in the region not of interest be zero is not enforced. Instead, the integral equation is "tested" at a discrete number of points along each surface where the equation is forced to hold. As the number of testing points is increased, the calculated scattered fields converge to the exact results. The method of moments can be used in cases where the extended boundary condition method fails. It requires, however, more computation time than the EBC.

3.1 General Formulation

Consider a plane wave incident upon a two-layer periodic surface described by $f_1(x) = f_1(x + P)$, $f_2(x) = f_2(x + P)$ with f_1 representing the upper surface, f_2 the lower surface and P denoting the period of the surface in the \hat{x} direction (see figure 1). The electric field of the incident wave is given by

$$\bar{E}_i = \hat{e}_i E_0 e^{i\bar{k}_i \cdot \bar{r}} \quad (7)$$

where \bar{k}_i denotes the incident wave vector and is equal to $\hat{x}k_{xi} + \hat{y}k_{yi} - \hat{z}k_{zi}$ and \hat{e}_i is the polarization of the electric field vector.

Since the structure is uniform in the \hat{y} direction, all the field components in regions 0, 1, and 2 will be phase matched to the same $\exp(ik_{yi}y)$ dependence. Thus, we can replace all the $\frac{\partial}{\partial y}$ terms in Maxwell's equations with ik_{yi} as is commonly done in waveguide theory (usually with the z dependence by convention.) Subsequent equations will thus have the $\exp(ik_{yi}y)$ dependence removed.

Maxwell's equations can now be simplified so that the \hat{x} and \hat{z} components of the electric and magnetic fields can be expressed as functions of the \hat{y} components of the fields as follows:

$$\bar{E}_{jx}(\bar{r}) = \frac{i}{k_j^2 - k_{yi}^2} [k_{yi} \nabla_s E_{jy}(\bar{r}) + \omega \mu_j \nabla_s \times \bar{H}_{jy}(\bar{r})] \quad (8)$$

$$\bar{H}_{jx}(\bar{r}) = \frac{i}{k_j^2 - k_{yi}^2} [k_{yi} \nabla_s H_{jy}(\bar{r}) - \omega \epsilon_j \nabla_s \times \bar{E}_{jy}(\bar{r})] \quad (9)$$

where $j = 0, 1, 2$ signifies regions 0, 1, or 2, respectively, ∇_s is the gradient operator that is transverse to the \hat{y} direction

$$\nabla_s = \hat{x} \frac{\partial}{\partial x} + \hat{z} \frac{\partial}{\partial z} \quad (10)$$

and $s = (x, z)$ indicates the transverse components of the fields for region j . The \hat{y} components of the electric and magnetic fields now satisfy the partial differential equations

$$(\nabla_s^2 + k_j^2 - k_{ys}^2)A_{jy} = 0 \quad (11)$$

where $A_{jy} = E_{jy}, H_{jy}$. Since ∇_s operates only in a two-dimensional space, the \hat{y} components of the electric and magnetic fields satisfy a two-dimensional wave equation. The Green's function for such an equation is given by

$$G_j(\bar{\rho}_s, \bar{\rho}'_s) = \frac{i}{4} H_0^{(1)}(k_{js} |\bar{\rho}_s - \bar{\rho}'_s|) \quad (12)$$

$$= \frac{i}{4\pi} \int_{-\infty}^{\infty} dk_z \frac{1}{k_{jz}} \times \exp[ik_z(x - x') + ik_{jz}|z - z'|] \quad (13)$$

where $j = 0, 1, 2$,

$$k_{js} = \sqrt{k_j^2 - k_{ys}^2} \quad (14)$$

$$k_{jz} = \sqrt{k_{js}^2 - k_z^2} \quad (15)$$

and

$$\bar{\rho}_s = \hat{x}x + \hat{z}z \quad (16)$$

The above square root functions are defined with the branch cut on the negative real axis.

Applying the scalar Green's function form of Huygens' principle to the top periodic surface and region 0 gives

$$\begin{aligned} E_{y1}(\bar{\rho}_s) &= \int_{-\infty}^{\infty} d\sigma' \{G_0(\bar{\rho}_s, \bar{\rho}'_s) \hat{n}_1 \cdot \nabla'_s E_{0y}(\bar{\rho}'_s) - E_{0y}(\bar{\rho}'_s) \hat{n}_1 \cdot \nabla'_s G_0(\bar{\rho}_s, \bar{\rho}'_s)\} \\ &= \begin{cases} E_{0y}(\bar{\rho}_s) & z > f_1(x) \\ 0 & z < f_1(x) \end{cases} \end{aligned} \quad (17)$$

where the \hat{y} dependence has been suppressed and

$$d\sigma' \hat{n}_j = \left[\hat{z} - \hat{x} \frac{df_j(x')}{dx'} \right] dx' \quad (18)$$

The above surface integral is over an infinite domain. However, the periodic properties of the surface fields can be used to reduce the integration domain to a single period. The surface fields have the property

$$\omega(\bar{\rho}_s + \hat{x}nP) = \omega(\bar{\rho}_s)e^{ik_{zs}nP} \quad (19)$$

where $\omega(\bar{\rho}_s)$ can be $E_{jy}(\bar{\rho}_s)$, $H_{jy}(\bar{\rho}_s)$ or their normal derivatives, n is an integer, and P is the period of the surface.

Following Chuang and Kong [5], a periodic Green's function can be derived using this property. This Green's function is

$$G_{jP}(\bar{\rho}_s, \bar{\rho}'_s) = \frac{-1}{2ik_{js}P} \sum_n \frac{1}{\beta_{jn}} \exp[ik_{js}\alpha_{jn}(x - x') + ik_{js}\beta_{jn}|z - z'|] \quad (20)$$

where

$$\alpha_{jn} = \frac{k_{zi} + n\frac{2\pi}{P}}{k_{js}} \quad (21)$$

$$\beta_{jn} = \begin{cases} (1 - \alpha_{jn}^2)^{1/2} & \alpha_{jn}^2 < 1 \\ i(1 - \alpha_{jn}^2)^{1/2} & \alpha_{jn}^2 > 1 \end{cases} \quad (22)$$

Now using the periodic Green's function in the scalar Huygens' principle formulation for each of the three regions yields

Region zero

$$\begin{aligned} E_{yz}(\bar{\rho}_s) - \int_{P(S_1)} d\sigma' \{G_{0P}(\bar{\rho}_s, \bar{\rho}'_s)\hat{n}_1 \cdot \nabla'_s E_{0y}(\bar{\rho}'_s) - E_{0y}(\bar{\rho}'_s)\hat{n}_1 \cdot \nabla'_s G_{0P}(\bar{\rho}_s, \bar{\rho}'_s)\} \\ = \begin{cases} E_{0y}(\bar{\rho}_s) & z > f_1(x) \\ 0 & z < f_1(x) \end{cases} \end{aligned} \quad (23)$$

$$\begin{aligned} H_{yz}(\bar{\rho}_s) - \int_{P(S_1)} d\sigma' \{G_{0P}(\bar{\rho}_s, \bar{\rho}'_s)\hat{n}_1 \cdot \nabla'_s H_{0y}(\bar{\rho}'_s) - H_{0y}(\bar{\rho}'_s)\hat{n}_1 \cdot \nabla'_s G_{0P}(\bar{\rho}_s, \bar{\rho}'_s)\} \\ = \begin{cases} H_{0y}(\bar{\rho}_s) & z > f_1(x) \\ 0 & z < f_1(x) \end{cases} \end{aligned} \quad (24)$$

Region one

$$\begin{aligned}
& \int_{P(S_1)} d\sigma' \{G_{1P}(\bar{\rho}_s, \bar{\rho}'_s) \hat{n}_1 \cdot \nabla'_s E_{1y}(\bar{\rho}'_s) - E_{1y}(\bar{\rho}'_s) \hat{n}_1 \cdot \nabla'_s G_{1P}(\bar{\rho}_s, \bar{\rho}'_s)\} - \\
& \int_{P(S_2)} d\sigma' \{G_{1P}(\bar{\rho}_s, \bar{\rho}'_s) \hat{n}_2 \cdot \nabla'_s E_{1y}(\bar{\rho}'_s) - E_{1y}(\bar{\rho}'_s) \hat{n}_2 \cdot \nabla'_s G_{1P}(\bar{\rho}_s, \bar{\rho}'_s)\} \\
& = \begin{cases} 0 & z > f_1(x) \\ E_{1y}(\bar{\rho}_s) & f_2(x) < z < f_1(x) \\ 0 & z < f_2(x) \end{cases} \quad (25)
\end{aligned}$$

$$\begin{aligned}
& \int_{P(S_1)} d\sigma' \{G_{1P}(\bar{\rho}_s, \bar{\rho}'_s) \hat{n}_1 \cdot \nabla'_s H_{1y}(\bar{\rho}'_s) - H_{1y}(\bar{\rho}'_s) \hat{n}_1 \cdot \nabla'_s G_{1P}(\bar{\rho}_s, \bar{\rho}'_s)\} - \\
& \int_{P(S_2)} d\sigma' \{G_{1P}(\bar{\rho}_s, \bar{\rho}'_s) \hat{n}_2 \cdot \nabla'_s H_{1y}(\bar{\rho}'_s) - H_{1y}(\bar{\rho}'_s) \hat{n}_2 \cdot \nabla'_s G_{1P}(\bar{\rho}_s, \bar{\rho}'_s)\} \\
& = \begin{cases} 0 & z > f_1(x) \\ H_{1y}(\bar{\rho}_s) & f_2(x) < z < f_1(x) \\ 0 & z < f_2(x) \end{cases} \quad (26)
\end{aligned}$$

Region two

$$\begin{aligned}
& \int_{P(S_2)} d\sigma' \{G_{2P}(\bar{\rho}_s, \bar{\rho}'_s) \hat{n}_2 \cdot \nabla'_s E_{2y}(\bar{\rho}'_s) - E_{2y}(\bar{\rho}'_s) \hat{n}_2 \cdot \nabla'_s G_{2P}(\bar{\rho}_s, \bar{\rho}'_s)\} \\
& = \begin{cases} E_{2y}(\bar{\rho}_s) & z < f_2(x) \\ 0 & z > f_2(x) \end{cases} \quad (27)
\end{aligned}$$

$$\begin{aligned}
& \int_{P(S_2)} d\sigma' \{G_{2P}(\bar{\rho}_s, \bar{\rho}'_s) \hat{n}_2 \cdot \nabla'_s H_{2y}(\bar{\rho}'_s) - H_{2y}(\bar{\rho}'_s) \hat{n}_2 \cdot \nabla'_s G_{2P}(\bar{\rho}_s, \bar{\rho}'_s)\} \\
& = \begin{cases} H_{2y}(\bar{\rho}_s) & z < f_2(x) \\ 0 & z > f_2(x) \end{cases} \quad (28)
\end{aligned}$$

where (Sl) indicates that the integration is performed over surface l .

Once the surface fields are determined, the fields in regions 0,1,and 2 can be obtained using these relations. At present, there are sixteen unknown vectors to be obtained: the \hat{y} components of the electric and magnetic fields at surface one for regions zero and one, the \hat{y} components of the electric and magnetic fields at surface two for regions one and two, and the normal derivatives of the \hat{y} component of the electric and magnetic fields for each of these surface-region combinations. Electric and magnetic field boundary conditions can be used at both surfaces to reduce the number of unknown vectors to eight.

3.2 Boundary Conditions

At both surfaces, the \hat{y} component of the electric and magnetic fields are tangential, and therefore must be continuous:

$$E_{0y} = E_{1y} \quad z = f_1(x) \quad (29)$$

$$H_{0y} = H_{1y} \quad (30)$$

$$E_{1y} = E_{2y} \quad z = f_2(x) \quad (31)$$

$$H_{1y} = H_{2y} \quad (32)$$

The components of the fields along the surface profile are also tangential and must be continuous. These relations can be written as:

$$\hat{n}_1 \times \bar{E}_{0s} = \hat{n}_1 \times \bar{E}_{1s} \quad z = f_1(x) \quad (33)$$

$$\hat{n}_1 \times \bar{H}_{0s} = \hat{n}_1 \times \bar{H}_{1s} \quad (34)$$

$$\hat{n}_2 \times \bar{E}_{1s} = \hat{n}_2 \times \bar{E}_{2s} \quad z = f_2(x) \quad (35)$$

$$\hat{n}_2 \times \bar{H}_{1s} = \hat{n}_2 \times \bar{H}_{2s} \quad (36)$$

Note that both the normal and the s component fields lie in the $x - z$ plane, so that $\hat{n}_j \times \bar{A}_s$ is a \hat{y} directed vector whose amplitude corresponds to the tangential component of the field along the surface profile. Following Chuang and Kong [5], the second set of boundary conditions can be written as:

$$\hat{y}(\hat{n}_1 \cdot \nabla_s E_{0y}) = c_0 \hat{n}_1 \times \nabla_s H_{1y} + c_2 \hat{y}(\hat{n}_1 \cdot \nabla_s E_{1y}) \quad z = f_1(x) \quad (37)$$

$$\hat{y}(\hat{n}_1 \cdot \nabla_s H_{0y}) = -d_0 \hat{n}_1 \times \nabla_s E_{1y} + d_2 \hat{y}(\hat{n}_1 \cdot \nabla_s H_{1y}) \quad (38)$$

$$\hat{y}(\hat{n}_2 \cdot \nabla_s E_{1y}) = c_1 \hat{n}_2 \times \nabla_s H_{2y} + c_3 \hat{y}(\hat{n}_2 \cdot \nabla_s E_{2y}) \quad z = f_2(x) \quad (39)$$

$$\hat{y}(\hat{n}_2 \cdot \nabla_s H_{1y}) = -d_1 \hat{n}_2 \times \nabla_s E_{2y} + d_3 \hat{y}(\hat{n}_2 \cdot \nabla_s H_{2y}) \quad (40)$$

where

$$c_0 = \left[\frac{k_{0s}^2}{k_{1s}^2} - 1 \right] \frac{k_{yi}}{\omega \epsilon_0} \quad c_1 = \left[\frac{k_{1s}^2}{k_{2s}^2} - 1 \right] \frac{k_{yi}}{\omega \epsilon_1} \quad (41)$$

$$c_2 = \frac{\epsilon_1 k_{0s}^2}{\epsilon_0 k_{1s}^2} \quad c_3 = \frac{\epsilon_2 k_{1s}^2}{\epsilon_1 k_{2s}^2} \quad (42)$$

$$d_0 = \left[\frac{k_{0s}^2}{k_{1s}^2} - 1 \right] \frac{k_{yi}}{\omega \mu_0} \quad d_1 = \left[\frac{k_{1s}^2}{k_{2s}^2} - 1 \right] \frac{k_{yi}}{\omega \mu_1} \quad (43)$$

$$d_2 = \frac{\mu_1 k_{0s}^2}{\mu_0 k_{1s}^2} \quad d_3 = \frac{\mu_2 k_{1s}^2}{\mu_1 k_{2s}^2} \quad (44)$$

These eight boundary conditions reduce the sixteen unknown vectors to eight. The remaining eight unknowns are then solved by expanding the surface fields in the Huygens' integral equations into a sum of unknown amplitude basis functions. The functions used in this expansion and the equations solved differ for the EBC and Moment methods; each method will be treated separately beginning with the EBC..

3.3 Extended Boundary Condition Method

If we substitute the expression for the periodic Green's function into the Huygens' Principle integral equations and factor out the unprimed exponential dependence, the equations reduce to:

Region zero

$$E_{0y}(\bar{\rho}_s) = E_{yi} + \sum_n b_{01n} \frac{e^{i\bar{k}_{0n}^+ \cdot \bar{\rho}_s}}{\sqrt{\beta_{0n}}} \quad z > f_{1(max)} \quad (45)$$

$$0 = E_{yi} - \sum_n a_{01n} \frac{e^{i\bar{k}_{0n}^- \cdot \bar{\rho}_s}}{\sqrt{\beta_{0n}}} \quad z < f_{1(min)} \quad (46)$$

$$H_{0y}(\bar{\rho}_s) = H_{yi} + \sum_n b_{01n}^{(h)} \frac{e^{i\bar{k}_{0n}^+ \cdot \bar{\rho}_s}}{\sqrt{\beta_{0n}}} \quad z > f_{1(max)} \quad (47)$$

$$0 = H_{yi} - \sum_n a_{01n}^{(h)} \frac{e^{i\bar{k}_{0n}^- \cdot \bar{\rho}_s}}{\sqrt{\beta_{0n}}} \quad z < f_{1(min)} \quad (48)$$

Region one

$$0 = \sum_n b_{11n} \frac{e^{i\bar{k}_{1n}^+ \cdot \bar{\rho}_s}}{\sqrt{\beta_{1n}}} + \sum_n b_{12n} \frac{e^{i\bar{k}_{1n}^+ \cdot \bar{\rho}_s}}{\sqrt{\beta_{1n}}} \quad z > f_{1(max)} \quad (49)$$

$$E_{1y}(\bar{\rho}_s) = \sum_n b_{12n} \frac{e^{i\bar{k}_{1n}^+ \cdot \bar{\rho}_s}}{\sqrt{\beta_{1n}}} + \sum_n a_{11n} \frac{e^{i\bar{k}_{1n}^- \cdot \bar{\rho}_s}}{\sqrt{\beta_{1n}}} \quad f_{2(max)} < z < f_{1(min)} \quad (50)$$

$$0 = \sum_n a_{11n} \frac{e^{i\bar{k}_{1n}^- \cdot \bar{\rho}_s}}{\sqrt{\beta_{1n}}} + \sum_n a_{12n} \frac{e^{i\bar{k}_{1n}^- \cdot \bar{\rho}_s}}{\sqrt{\beta_{1n}}} \quad z < f_{2(min)} \quad (51)$$

$$0 = \sum_n b_{11n}^{(h)} \frac{e^{i\bar{k}_{1n}^+ \cdot \bar{\rho}_s}}{\sqrt{\beta_{1n}}} + \sum_n b_{12n}^{(h)} \frac{e^{i\bar{k}_{1n}^+ \cdot \bar{\rho}_s}}{\sqrt{\beta_{1n}}} \quad z > f_{1(max)} \quad (52)$$

$$H_{1y}(\bar{\rho}_s) = \sum_n b_{12n}^{(h)} \frac{e^{i\bar{k}_{1n}^+ \cdot \bar{\rho}_s}}{\sqrt{\beta_{1n}}} + \sum_n a_{11n}^{(h)} \frac{e^{i\bar{k}_{1n}^- \cdot \bar{\rho}_s}}{\sqrt{\beta_{1n}}} \quad f_{2(max)} < z < f_{1(min)} \quad (53)$$

$$0 = \sum_n a_{11n}^{(h)} \frac{e^{i\bar{k}_{1n}^- \cdot \bar{\rho}_s}}{\sqrt{\beta_{1n}}} + \sum_n a_{12n}^{(h)} \frac{e^{i\bar{k}_{1n}^- \cdot \bar{\rho}_s}}{\sqrt{\beta_{1n}}} \quad z < f_{2(min)} \quad (54)$$

Region two

$$E_{2y}(\bar{\rho}_s) = \sum_n b_{22n} \frac{e^{i\bar{k}_{2n}^+ \cdot \bar{\rho}_s}}{\sqrt{\beta_{2n}}} \quad z < f_{2(min)} \quad (55)$$

$$0 = -\sum_n a_{22n} \frac{e^{i\bar{k}_{2n}^- \cdot \bar{\rho}_s}}{\sqrt{\beta_{0n}}} \quad z > f_{2(max)} \quad (56)$$

$$H_{2y}(\bar{\rho}_s) = \sum_n b_{22n}^{(h)} \frac{e^{i\bar{k}_{2n}^+ \cdot \bar{\rho}_s}}{\sqrt{\beta_{2n}}} \quad z < f_{2(min)} \quad (57)$$

$$0 = -\sum_n a_{22n}^{(h)} \frac{e^{i\bar{k}_{2n}^- \cdot \bar{\rho}_s}}{\sqrt{\beta_{2n}}} \quad z > f_{2(max)} \quad (58)$$

where the $|z - z'|$ expression in the periodic Green's function has been replaced by $z - z'$ when the observation point is above the surface, $z' - z$ when the observation point is below the surface. In the above equations,

$$\bar{k}_{jn}^\pm = \hat{x} k_{jz} \alpha_{jn} \pm \hat{z} k_{jz} \beta_{jn} \quad (59)$$

$$b_{jln} = \frac{1}{2ik_{jz}P} \int_{P(SI)} d\sigma' \left\{ \frac{e^{-i\bar{k}_{jn}^+ \cdot \bar{\rho}_s(z')}}{\sqrt{\beta_{jn}}} \hat{n}_l \cdot \nabla'_s E_{jv}(\bar{\rho}'_s) - E_{jv}(\bar{\rho}'_s) \hat{n}_l \cdot \nabla'_s \frac{e^{-i\bar{k}_{jn}^+ \cdot \bar{\rho}_s(z')}}{\sqrt{\beta_{jn}}} \right\} \quad (60)$$

$$a_{jln} = \frac{-1}{2ik_{js}P} \int_{P(SI)} d\sigma' \left\{ \frac{e^{-i\vec{k}_{jn}^+ \cdot \vec{\rho}_s(x')}}{\sqrt{\beta_{jn}}} \hat{n}_l \cdot \nabla'_s E_{jy}(\vec{\rho}'_s) - E_{jy}(\vec{\rho}'_s) \hat{n}_l \cdot \nabla'_s \frac{e^{-i\vec{k}_{jn}^+ \cdot \vec{\rho}_s(x')}}{\sqrt{\beta_{jn}}} \right\} \quad (61)$$

and $b_{jln}^{(h)}$ and $a_{jln}^{(h)}$ have the same form as their electric field counterparts with E_{jy} replaced by H_{jy} . We now recognize that the scattered field in region 0 is composed of a discrete set of plane waves traveling in the directions indicated by \vec{k}_{0n}^+ . These plane waves are known as the Floquet modes; the amplitude of the n th reflected mode is determined by b_{01n} .

For the extended boundary condition method, we use the equations which involve the region of no interest for each region. These are equations (46), (48), (49), (51), (52), (54), (56), and (58). These eight equations will uniquely determine the eight unknown surface field vectors. Once the surface fields are determined, the remaining equations are used to calculate the scattered field in each of the three regions.

Following Chuang and Kong [5], a Fourier series expansion is used for each of the unknown field quantities as follows:

Surface one

$$E_{1y}[\vec{\rho}_s(x)] = \sum_n 2\alpha_n^T \exp \left[ik_{xi}x + i\frac{2\pi n}{P}x \right] \quad (62)$$

$$d\sigma \hat{n}_1 \cdot \nabla_s E_{1y}[\vec{\rho}_s(x)] = ik_{1s}dx \sum_n 2\beta_n^T \exp \left[ik_{xi}x + i\frac{2\pi n}{P}x \right] \quad (63)$$

$$H_{1y}[\vec{\rho}_s(x)] = \sum_n 2\gamma_n^T \exp \left[ik_{xi}x + i\frac{2\pi n}{P}x \right] \quad (64)$$

$$d\sigma \hat{n}_1 \cdot \nabla_s H_{1y}[\vec{\rho}_s(x)] = ik_{1s}dx \sum_n 2\delta_n^T \exp \left[ik_{xi}x + i\frac{2\pi n}{P}x \right] \quad (65)$$

Surface two

$$E_{2y}[\vec{\rho}_s(x)] = \sum_n 2\alpha_n^B \exp \left[ik_{xi}x + i\frac{2\pi n}{P}x \right] \quad (66)$$

$$d\sigma \hat{n}_2 \cdot \nabla_s E_{2y}[\vec{\rho}_s(x)] = ik_{2s}dx \sum_n 2\beta_n^B \exp \left[ik_{xi}x + i\frac{2\pi n}{P}x \right] \quad (67)$$

$$H_{2y}[\vec{\rho}_s(x)] = \sum_n 2\gamma_n^B \exp \left[ik_{xi}x + i\frac{2\pi n}{P}x \right] \quad (68)$$

$$d\sigma \hat{n}_2 \cdot \nabla_s H_{2y} [\bar{\rho}_s(x)] = ik_{2s} dx \sum_n 2\delta_n^B \exp \left[ik_{2s}x + i\frac{2\pi n}{P}x \right] \quad (69)$$

Substituting the above expressions into the eight equations and using the property

$$d\sigma \hat{n}_j \times \nabla_s H_{jy}(x, z(x)) = \hat{y} dx \left(\frac{\partial H_{jy}}{\partial x} + \frac{dz}{dx} \frac{\partial H_{jy}}{\partial z} \right) = \hat{y} dx \left(\frac{dH_{jy}}{dx} \right) \quad (70)$$

leads to the coupled matrix equation of Appendix A. Truncating the Fourier series of the surface field unknowns results in a finite matrix equation which can be solved to obtain the surface field unknowns. The upward going field amplitudes are then calculated to be

$$\bar{b}_{01} = -c_0 \bar{C}_1^+ \gamma^T - c_2 \frac{k_{1s}}{k_{0s}} \bar{B}_1^+ \beta^T - \bar{A}_1^+ \alpha^T \quad (71)$$

$$\bar{b}_{01}^{(h)} = d_0 \bar{C}_1^+ \alpha^T - d_2 \frac{k_{1s}}{k_{0s}} \bar{B}_1^+ \delta^T - \bar{A}_1^+ \gamma^T \quad (72)$$

and the downward going field amplitudes in region 2 are

$$\bar{a}_{22} = \bar{E}_2^- \beta^B + \bar{D}_2^- \alpha^B \quad (73)$$

$$\bar{a}_{22}^{(h)} = \bar{E}_2^- \delta^B + \bar{D}_2^- \gamma^B \quad (74)$$

The matrices in the above equations are as described in Appendix A. The above coefficients are the amplitudes of the \hat{y} components of the scattered and transmitted electric and magnetic fields. The \hat{x} and \hat{z} components can be calculated from equations (8) and (9). The scattered plane waves in region zero propagate along the directions determined by \bar{k}_{0n}^+ , while the transmitted plane waves in region two travel along the directions of \bar{k}_{2n}^- .

Once the amplitudes of the scattered modes are calculated, the emissivity of the surface can be obtained by integrating the total power reflected over the upper hemisphere and then applying Kirchhoff's law to obtain the emissivity corresponding to the polarization of the incident field. For the n^{th} propagating scattered Floquet mode, the reflectivity is given by power transmitted in the \hat{z} direction divided by the incident power and is found in [5] to be:

$$r_n = \frac{|b_{01n}|^2 + |\eta_0 b_{01n}^{(h)}|^2}{|a_{010}|^2 + |\eta_0 a_{010}^{(h)}|^2} \quad (75)$$

where the a_{010} and $a_{010}^{(h)}$ are as defined in Appendix A. The brightness temperature of the surface is then given by

$$T_{Ba} = T_{phys}(1 - \sum_n r_n) \quad (76)$$

where the sum is over the propagating modes reflected for an incident wave polarized in the a direction.

3.4 Method of Moments

A second method for solving the Huygens' integral equations for a two-layer periodic surface is the method of moments. The use of the method of moments for computing scattering from a single-layer periodic surface has been presented by Veysoglu et al [2]; these methods will be extended for the two-layer periodic surface in this section.

We begin with the integral equations presented in the general formulation section and the periodic Green's function. We will also use a second form of the periodic Green's function in the calculations

$$G_{jP}(\bar{\rho}, \bar{\rho}') = \frac{i}{4} \sum_{m=-\infty}^{\infty} H_0^{(1)}(k_{jz} \sqrt{[x - (x' + mp)]^2 + (z - z')^2}) \exp(ik_{0x}mp) \quad (77)$$

in addition to the sum of exponentials form used in the EBC method. The eight surface field unknowns in the integral equations are now expanded into sums of unknown amplitude "pulse" functions as follows:

Surface one

$$E_{1y}(\bar{r}) = \sum_n a_n P_n(\bar{r}) \quad (78)$$

$$\hat{n}_1 \cdot \nabla_s E_{1y}(\bar{r}) = \sum_n b_n P_n(\bar{r}) \quad (79)$$

$$H_{1y}(\bar{r}) = \sum_n c_n P_n(\bar{r}) \quad (80)$$

$$\hat{n}_1 \cdot \nabla_s H_{1y}(\bar{r}) = \sum_n d_n P_n(\bar{r}) \quad (81)$$

Surface two

$$E_{2y}(\bar{r}) = \sum_n e_n P_n(\bar{r}) \quad (82)$$

$$\hat{n}_2 \cdot \nabla_s E_{2y}(\bar{r}) = \sum_n f_n P_n(\bar{r}) \quad (83)$$

$$H_{2y}(\bar{r}) = \sum_n g_n P_n(\bar{r}) \quad (84)$$

$$\hat{n}_2 \cdot \nabla_s H_{2y}(\bar{r}) = \sum_n h_n P_n(\bar{r}) \quad (85)$$

where

$$P_n(\bar{r}) = \begin{cases} 1 & \frac{(n-1)P}{N} < x < \frac{nP}{N} \\ 0 & \text{otherwise} \end{cases} \quad (86)$$

and N is the total number of basis (pulse) functions used.

Instead of solving the equations with right-hand-sides of zero, as was done in the EBC method, the method of moments uses the equations with right-hand-sides corresponding to the fields in the region of interest. These six equations are "tested" at a discrete set of points along the surface upon which the integral is performed where the integral equations are forced to hold. The missing two equations needed to match the eight unknown functions are obtained from testing the integral equations for region one on both surfaces one and two. The testing points are chosen to lie in the center of the pulse basis functions described above. The integral equations now reduce to the matrix equation given in the Appendix B.

Note that this method will require the integration of the singularity in the periodic Green's function when the testing point and integration range overlap. For these "self" terms of the matrices, an asymptotic expression for the Hankel function of a small argument is used and analytically integrated. The integral expression proposed by Veysoglu et al [2] is also used to speed up the convergence of the evaluation of the Hankel function sum in the periodic Green's function. After solving the matrix equation to determine the surface fields, the coefficients of the reflected and transmitted Floquet modes can be calculated. If the reflected fields in region zero are written as

$$E_{0y}^* = \sum_n b_n e^{i\mathbf{k}_{0n}^* \cdot \bar{\rho}} \quad (87)$$

$$H_{0y}^* = \sum_n b_n^{(h)} e^{i\mathbf{k}_{0n}^* \cdot \bar{\rho}} \quad (88)$$

and the transmitted fields in region two as

$$E_{2y}^t = \sum_n A_n e^{i\bar{k}_{2n}^- \cdot \bar{\rho}} \quad (89)$$

$$H_{2y}^t = \sum_n A_n^{(h)} e^{i\bar{k}_{2n}^- \cdot \bar{\rho}} \quad (90)$$

the coefficients are given in terms of the surface fields by

$$b_n = \frac{1}{2ik_{0z}P} \int_{P(S1)} dS \left[\frac{e^{-i\bar{k}_{0n}^- \cdot \bar{\rho}}}{\beta_n} \hat{n}_1 \cdot \nabla_s E_{0y}(\bar{\rho}) - E_{0y}(\bar{\rho}) \hat{n}_1 \cdot \nabla_s \frac{e^{-i\bar{k}_{0n}^- \cdot \bar{\rho}}}{\beta_n} \right] \quad (91)$$

$$b_n^{(h)} = \frac{1}{2ik_{0z}P} \int_{P(S1)} dS \left[\frac{e^{-i\bar{k}_{0n}^- \cdot \bar{\rho}}}{\beta_n} \hat{n}_1 \cdot \nabla_s H_{0y}(\bar{\rho}) - H_{0y}(\bar{\rho}) \hat{n}_1 \cdot \nabla_s \frac{e^{-i\bar{k}_{0n}^- \cdot \bar{\rho}}}{\beta_n} \right] \quad (92)$$

$$A_n = \frac{1}{2ik_{2z}P} \int_{P(S2)} dS \left[\frac{e^{-i\bar{k}_{2n}^- \cdot \bar{\rho}}}{\beta_n} \hat{n}_2 \cdot \nabla_s E_{2y}(\bar{\rho}) - E_{2y}(\bar{\rho}) \hat{n}_2 \cdot \nabla_s \frac{e^{-i\bar{k}_{2n}^- \cdot \bar{\rho}}}{\beta_n} \right] \quad (93)$$

$$A_n^{(h)} = \frac{1}{2ik_{2z}P} \int_{P(S2)} dS \left[\frac{e^{-i\bar{k}_{2n}^- \cdot \bar{\rho}}}{\beta_n} \hat{n}_2 \cdot \nabla_s H_{2y}(\bar{\rho}) - H_{2y}(\bar{\rho}) \hat{n}_2 \cdot \nabla_s \frac{e^{-i\bar{k}_{2n}^- \cdot \bar{\rho}}}{\beta_n} \right] \quad (94)$$

where \bar{k}_{jn}^- is defined as in the EBC section.

As with the EBC, once the mode amplitudes are determined, the emissivity can be found by integrating the total power reflected over the upper hemisphere and then applying Kirchhoff's Law. Note that the method of moments does not suffer from the problems of the EBC when the height-to-period ratio becomes too large. A larger number of basis functions is required and the calculations take longer to perform, but the method ultimately yields an accurate result.

3.5 Comparison of Methods

Both the EBC and MOM methods were used to perform a theoretical analysis of the surface in the experiment. Figure 2 is a plot of the four polarimetric brightness temperatures calculated by both the EBC and MOM at polar angle 20° . Also shown in these plots are the corresponding brightness temperatures for a periodic water surface without the fiberglass layer on top. These calculations are for the experimental parameters described in the next section, namely a 6.8 cm period quasi-sinusoidal surface (described in the next section) with a peak-to-peak height of 1.4 cm and thickness 1.75 mm, dielectric constant $3.1 + i0.05$ of the fiberglass layer, and dielectric constant $64 + i29$ for the water, assuming a physical temperature of 300 K. The EBC and MOM results are seen to agree, indicating that the surface slope limitations of the EBC are not being exceeded and that the numerical resolution of the method of moments code is adequate. The MOM code, however, was found to require approximately ten times more CPU time than the EBC, primarily due to the summation of the slowly convergent periodic Green's function. The more efficient EBC method was thus used for the rest of the theoretical calculations presented in this paper. It is also seen that the effect of the layer is to increase T_{Bh} , T_{Bv} , and T_{Bp} by approximately 30K over the single-layer brightnesses, but the effect on U_B is small due to cancellation of this increase when the brightnesses in the three polarizations are used to compute U_B . Finally, the characteristic "jumps" in brightness temperature for an infinite periodic surface due to the transition of a Floquet mode from propagating to non-propagating are seen in the T_{Bh} curve. Note that the exact shape of the curve may not be the same as that of Figure 2, as the curve was linearly interpolated between the calculated points every 15 degrees in azimuth.

4 Experiment Setup

To form the periodic water surface, a corrugated sheet of fiberglass 1.32 m x 1.22 m x 1.75 mm thick was placed on top of a 1.83 m side square pool of fresh water of 0.23 m

depth. The corrugation of the sheet had a sinusoidal profile on its lower surface, and had a uniform thickness normal to this surface, which defined the upper profile. This upper surface is thus a slight deviation from a true sinusoid; we will describe this surface as quasi-sinusoidal. The height and period of the sinusoidal lower profile were 1.4 cm peak-to-peak and 6.8 cm respectively. To prevent water from flowing over the edges, a styrofoam border approximately 3 cm high was glued around the surface.

The temperature of the water was measured around the surface in the experiment and found to be $22.5^\circ \pm 1.5^\circ$ C throughout the experiment. As fresh water was used, this corresponds to an average dielectric constant of $64 + i29$ at 10 GHz over this temperature range [7]. The dielectric constant of the fiberglass layer was measured using a network analyzer technique [6] from 12 to 18 GHz and found to be $3.1 \pm 0.1 + i(0.05 \pm 0.05)$ over this entire band. An accurate calibration kit was not available for the network analyzer at 10 GHz; however, due to the constant nature of the dielectric constant from 12 to 18 GHz, it was assumed that the dielectric constant was the same at 10 GHz.

The radiometer used in the experiment is the same as that used in [3]. It operates at 10 GHz with a 200-MHz RF bandwidth, -3 mV/K sensitivity, ± 1 K precision, and a pyramidal (standard gain) horn of 30° beamwidth. The radiometer was mounted on a tripod at an elevation of 1.7 m above the pool surface and directed toward the surface along a direction determined by the azimuthal angle, ϕ , and the polar angle, θ (see Figure 1). The radiometer was calibrated by viewing an absorber whose physical temperature was known for the hot load, and by viewing the sky at a set of angles for the cold load. Since the measured sky voltage can be expressed as a function of polar angle, the points measured can be extrapolated to obtain a radiometer voltage corresponding to brightness temperature $3K$. This voltage is then used as the cold reference for the calibration.

Observations of the periodic surface were made as a function of azimuthal angle, which was varied by rotating the periodic surface in the pool so that the background noise contribution from the antenna sidelobes would remain constant through a set of measurements.

The horn of this single polarization radiometer was rotated to produce measurements of T_{Bh} , T_{Bv} , and T_{Bp} . Measurements of $T_{B\theta}$ were not possible with this radiometer; however, the V_B brightness was not predicted to be significant.

5 Estimation of Noise Contribution

The contribution of background noise to the measured antenna temperature for the periodic surface can be large: noise from the antenna sidelobes and from reflections of sky brightness off the surface both contribute to error in the measurements. Since this background noise could not be easily eliminated from the experiment, estimates of the background contribution were made so that the noise could later be removed. The contribution of the background noise was estimated by measuring the brightness temperature of a flat water surface alone and by measuring the brightness temperature of a reflector in the pool which was the same size as the periodic surface. The theoretical results for both of these cases are known; thus, these measurements form a sort of two-point calibration for the periodic surface when it is in the pool.

Consider the case of the observation of the water in the pool alone. The measured brightness temperature, T_{flatM} , consists of contributions from the water surface, T_{flat} , from the ground beside the pool and the sides of the pool, T_{side} , and from reflections of the sky temperature, T_{sky} , off the pool. The contribution of the reflections of the sky temperature from the ground beside the pool is neglected. If we assume that there is no variation in these temperatures with the incidence angle, then the relationship between these variables can be written as:

$$T_{flatM} = T_{flat}(1 - f_s) + T_{sky}(1 - f_s)(1 - T_{flat}/T_{Pwat}) + T_{side}f_s \quad (95)$$

where f_s represents the fraction of the antenna pattern that does not view the pool and T_{Pwat} is the physical temperature of the water in the pool. Measured values of f_s ranged from 3 to 18 percent through the experiment. Both T_{sky} and T_{side} were obtained from the

experiment at angles corresponding to the specular reflection for the sky temperature and direct incidence for the ground temperature.

Next consider the case of a reflector in the pool the same size and at the same location as the periodic surface. The brightness temperature measured, T_{reflM} , consists of the reflection of the sky temperature over the reflector surface, the flat water surface temperature over the remainder of the pool and the reflection of the sky temperature from this portion of the surface, and the ground contribution. This can be expressed as:

$$\begin{aligned} T_{reflM} = & T_{sky}f_r + T_{sky}(1 - f_r - f_s)(1 - T_{flat}/T_{Pwat}) \\ & + T_{flat}(1 - f_r - f_s) + T_{side}f_s \end{aligned} \quad (96)$$

$$= T_{flatM} + T_{flat}f_r(T_{sky}/T_{Pwat} - 1) \quad (97)$$

where f_r is the fraction of the antenna pattern that views the reflector surface, which was found to range from 50 to 74 percent through the experiment. A further assumption that the physical temperature of the water and the background sky temperature are the same in the flat surface and reflector measurements is made in the second equality.

Finally, consider the case of the periodic surface in the pool. The measured temperature, T_{surfM} , consists of contribution from the periodic surface, the flat water in the pool, sky reflections off the pool area, and the side contribution. The reflections of sky temperature off the periodic surface are determined by its Floquet modes; however, since the sky temperature is assumed uniform, this reduces to the same case as that of a specular reflector. The measured temperature can be expressed as:

$$\begin{aligned} T_{surfM} = & T_{surf}f_r + T_{sky}f_r(1 - T_{surf}/T_{Pwat}) + T_{flat}(1 - f_r - f_s) \\ & + T_{sky}(1 - T_{flat}/T_{Pwat})(1 - f_r - f_s) + T_{side}f_s \end{aligned} \quad (98)$$

$$= T_{reflM} + T_{surf}f_r(1 - T_{sky}/T_{Pwat}) \quad (99)$$

These three equations can be used to solve for T_{surf} , the periodic surface brightness

temperature averaged over the fraction of the antenna pattern on the surface:

$$T_{surf} = \frac{T_{flat}}{T_{flatM} - T_{reflM}}(T_{surfM} - T_{reflM}) \quad (100)$$

This brightness temperature has the effects of both the reflections of the sky temperature off the surface and the antenna field of view outside of the periodic surface removed.

This calibration procedure increases the effect of the radiometer measurement uncertainty in the final calculated T_{surf} to approximately 3 K. The assumptions made in the above equations also contribute to the error in the experiment. A theoretical study in which the brightness contributions of the water around the surface and the sky temperature were estimated by integrating the angularly varying T_{flat} and T_{sky} over a theoretical antenna pattern indicated that the use of the specular T_{flat} and T_{sky} values were valid to within 2 K. A bias in both of these values would produce a systematic error of less than 5 K. One remaining possible source of error is the possibility of the close-to-the-horizon Floquet modes of the periodic surface imaging something with a higher brightness temperature than the sky. Note that the U_B parameter is fairly insensitive to any systematic error in the calibration used. Since systematic error will tend to affect all three polarizations in a similar manner, the effects tend to cancel out, leaving U_B unaffected.

The results presented in Section 6 for the measurements of periodic surface brightness temperatures were obtained using the above technique.

6 Experimental Results

Figure 3 is a plot of the measured brightness temperatures before and after the noise removal calibration for $\theta = 20^\circ$, normalized to a constant physical temperature of 300 K. Plotted are the measured brightness temperatures T_{Bh} , T_{Bv} , U_B , and T_{Bp} . The U_B brightness temperature is obtained from $U_B = T_{Bh} + T_{Bv} - 2T_{Bp}$. This formula is opposite in sign to that previously given due to the fact that the radiometer polarization basis was actually rotated to -45° in the experiment. It is observed from the experiment that, in general, the U_B value approaches a maximum absolute value at $\phi = -45^\circ$ and approaches zero at

$\phi = -90^\circ$ and $\phi = 0^\circ$. This shows that the U_B parameter is sensitive to the azimuthal direction of a periodic water surface. It is also observed that the noise removal calibration has its largest effects near $\phi = -45^\circ$, at which the lowest amount of the radiometer beam pattern was on the surface.

Figure 4 plots the measured brightness temperatures at $\theta = 30^\circ$ before and after the noise removal calibration. The same trends in the U_B temperature are observed as in Figure 3. Note that the noise removal technique has a larger effect on the data for this case, due to the fact that less of the antenna pattern was on the surface for the higher polar angle.

7 Comparison with Plane Wave Calculations

Figures 5 and 6 are plots of the measurement results and the theoretically predicted brightness temperatures for polar angles 20° and 30° , respectively, normalized to a constant physical temperature of 300 K. The theoretical values plotted were obtained using the modified version of the Extended Boundary Condition method. The theoretical and experimental results are seen to have the same general trends in all both of these figures. However, the abrupt changes in the theoretical curves due to the transition of one Floquet mode of the periodic surface from propagating to non-propagating are not seen in the experimental results. The primary reason for this discrepancy is considered in the next section.

8 Antenna Pattern Effects

One source of the differences between the theoretical and experimental results presented in the last section is the effect of the radiometer antenna pattern. The theoretical results presented in the last section assumed a plane wave incidence or, for the passive case, an antenna pattern which viewed only one angle (a delta function in theta and phi at the observation angle.) Since the antenna used in the experiment actually samples a range of angles over its pattern, this effect should be taken into account in order to more accurately

model the experiment. To take the antenna pattern effects into account, the observed antenna temperature, T_A , can be written as:

$$T_A = \frac{\iint T_B(\theta, \phi) G(\theta, \phi) d\Omega}{\iint G(\theta, \phi) d\Omega} \quad (101)$$

where $G(\theta, \phi)$ is the power gain pattern of the antenna and the integrals are performed over all space. This expression assumes that the emission from different directions is uncorrelated, since the brightness temperatures (powers) are summed directly.

The gain pattern used for the calculations was obtained from [8], using the pattern for a pyramidal horn with the measured antenna dimensions of $b = 5.7$ cm by $a = 7$ cm for the aperture dimension and $l_E = 10$ cm and $l_H = 8.9$ cm for the corresponding flare lengths of the horn.

Figures 7 and 8 are plots of the measurement results and the theoretically predicted values for the experiment at polar angles 20° and 30° , respectively. The theoretical values plotted were obtained using the modified version of the Extended Boundary Condition method. These theoretical results were also averaged noncoherently over 81 points in the three-dimensional calculated antenna pattern for the pyramidal horn used in the experiment, which tends to smooth out the abrupt changes obtained for plane wave incidence in Section 7.

Good agreement is observed between the theory and experiment, indicating that the background noise removal procedure was reasonable. However, there is a slight bias of the experimental results above the theoretical predictions on the average. One possible source of this error is the dielectric constant value for the fiberglass surface used in the experiment, which could be slightly higher at 10 GHz than the measured value at 12.4 GHz. An increase in the real part of this value to 3.2 indicates that this could increase the theoretical predictions by approximately 5 K or 0.017 emissivity. A second possible source of the error is the use of the specular values for T_{flat} and T_{sky} as discussed in section 5. This could also contribute approximately 5 K or 0.017 emissivity variation. Finally, the imaging of a brightness source other than the sky by the Floquet modes of the

periodic surface would tend to increase the experimental brightness temperatures above the theoretical predictions. However, the area in which the experiment was performed was clear to about ten degrees above the horizon. Only the azimuthal angles -90 , -15 , 0 , and 15 are theoretically predicted to have modes this close to the horizon.

9 Conclusion

We have demonstrated in this paper that the U_B parameter exists for a two-layer periodic water surface and can approach brightnesses exceeding 30 K at X band. We have also shown that the U_B parameter is fairly insensitive to the effects of the fiberglass layer and the measurement uncertainties in the experiment as an indicator of surface azimuthal direction. Although the periodic water surface is an extremely simplified model of an actual ocean surface, this experiment further strengthens the idea of using passive polarimetry to infer wind direction over the ocean. Further research into this area and into other applications of passive polarimetric remote sensing will continue.

Acknowledgements This work was supported in part by ONR Grant N00014-92-J-1616, NASA grant NAGW-1617, and a National Science Foundation Graduate Research Fellowship. The authors would like to thank M. A. Tassoudji of MIT for assistance with surface construction and M. E. Veysoglu of MIT and S. H. Yueh of JPL for helpful discussions on the theoretical formulation.

REFERENCES

- [1] Tsang, L., "Polarimetric passive microwave remote sensing of random discrete scatterers and rough surfaces," *J. Electromag. Waves Applic.*, Vol. 5, No. 1, 41-57, 1991.
- [2] Veysoglu, M. E., H. A. Yueh, R. T. Shin and J. A. Kong, "Polarimetric passive remote sensing of periodic surfaces," *J. Electromag. Waves Applic.*, Vol. 5, No. 3, 267-280, 1991.
- [3] Nghiem, S. V., M. E. Veysoglu, J. A. Kong, R. T. Shin, K. O'Neill, and A. W. Lohanick, "Polarimetric passive remote sensing of a periodic soil surface: microwave measurements and analysis," *J. Electromag. Waves Applic.*, Vol. 5, No. 9, 997-1005, 1991.
- [4] Tsang, L., J. A. Kong, and R. T. Shin, *Theory of Microwave Remote Sensing*, John Wiley, New York, 1985.
- [5] Chuang, S. L. and J. A. Kong, "Wave scattering from a periodic dielectric surface for a general angle of incidence," *Radio Science*, Vol. 17, No. 3, 545-557, 1982.
- [6] Hewlett Packard Co., "Measuring the dielectric constant of solids with the HP 8510 network analyzer," Product Note 8510-3.
- [7] Klein, L. A. and C. T. Swift, "An improved model for the dielectric constant of sea water at microwave frequencies," *IEEE Trans. Ant. Propag.*, AP-25, 104-111, 1977.
- [8] Jull, E. V., *Aperture Antennas and Diffraction Theory*, P. Peregrinus, New York, 55-60, 1981.

[9] Harrington, R. F., *Field Computation by Moment Methods*, Macmillan, New York, 1968.

[10] Garcia, N., V. Celli, N. Hill, and N. Cabrera, "Ill conditioned matrices in the scattering of waves from hard corrugated surfaces," *Physical Review B*, Vol. 18, No. 10, 5184-89, 1978.

Appendix A: EBC Coupled Matrix Equation

The matrix equation of the EBC can be written as:

$$\begin{bmatrix} A_0^- & c_2 \frac{k_{1A}}{k_{0s}} B_0^- & c_0 C_0^- & 0 & 0 & 0 & 0 & 0 \\ -d_0 C_0^- & 0 & A_0^- & d_2 \frac{k_{1A}}{k_{0s}} B_0^- & 0 & 0 & 0 & 0 \\ A_1^+ & B_1^+ & 0 & 0 & -D_1^+ & -c_3 \frac{k_{2A}}{k_{1s}} B_1^+ & -c_1 P_1^+ & 0 \\ 0 & 0 & A_1^+ & B_1^+ & d_1 P_1^+ & 0 & -D_1^+ & -d_3 \frac{k_{2A}}{k_{1s}} B_1^+ \\ A_1^- & B_1^- & 0 & 0 & -D_1^- & -c_3 \frac{k_{2A}}{k_{1s}} B_1^- & -c_1 P_1^- & 0 \\ 0 & 0 & A_1^- & B_1^- & d_1 P_1^- & 0 & -D_1^- & -d_3 \frac{k_{2A}}{k_{1s}} B_1^- \\ 0 & 0 & 0 & 0 & D_2^+ & B_2^+ & 0 & 0 \\ 0 & 0 & 0 & 0 & 0 & 0 & D_2^+ & B_2^+ \end{bmatrix} \begin{bmatrix} a^T \\ \beta^T \\ \gamma^T \\ \delta^T \\ a^B \\ \beta^B \\ \gamma^B \\ \delta^B \end{bmatrix} = \begin{bmatrix} a_{01}^{(A)} \\ a_{01}^{(B)} \\ 0 \\ 0 \\ 0 \\ 0 \\ 0 \\ 0 \end{bmatrix} \quad (102)$$

where

$$\begin{aligned} [A_j^\pm]_{mn} &= \frac{1}{ik_{js}P} \int_{P(S1)} d\sigma \hat{n}_1 \cdot \nabla_s \frac{e^{-ik_{jm}^\pm \cdot \vec{\rho}_s(x)}}{\sqrt{\beta_{jm}}} \exp \left[ik_{zi}x + i\frac{2n\pi}{P}x \right] \\ &= \frac{-1 + \alpha_{jm}\alpha_{jn}}{P(\pm\beta_{jm})\sqrt{\beta_{jm}}} \int_{P(S1)} dx \exp \left[-i(m-n)\frac{2\pi}{P}x - ik_{js}(\pm\beta_{jm})f_1(x) \right] \end{aligned} \quad (103)$$

$$\begin{aligned} [B_j^\pm]_{mn} &= \frac{-1}{P} \int_{P(S1)} dx \frac{e^{-ik_{jm}^\pm \cdot \vec{\rho}_s(x)}}{\sqrt{\beta_{jm}}} \exp \left[ik_{zi}x + i\frac{2n\pi}{P}x \right] \\ &= \frac{-1}{P\sqrt{\beta_{jm}}} \int_{P(S1)} dx \exp \left[-i(m-n)\frac{2\pi}{P}x - ik_{js}(\pm\beta_{jm})f_1(x) \right] \end{aligned} \quad (104)$$

$$[C_j^\pm]_{mn} = \alpha_{jn} [B_j^\pm]_{mn} \quad (105)$$

$$\begin{aligned} [D_j^\pm]_{mn} &= \frac{1}{ik_{js}P} \int_{P(S2)} d\sigma \hat{n}_2 \cdot \nabla_s \frac{e^{-ik_{jm}^\pm \cdot \vec{\rho}_s(x)}}{\sqrt{\beta_{jm}}} \exp \left[ik_{zi}x + i\frac{2n\pi}{P}x \right] \\ &= \frac{-1 + \alpha_{jm}\alpha_{jn}}{P(\pm\beta_{jm})\sqrt{\beta_{jm}}} \int_{P(S2)} dx \exp \left[-i(m-n)\frac{2\pi}{P}x - ik_{js}(\pm\beta_{jm})f_2(x) \right] \end{aligned} \quad (106)$$

$$\begin{aligned} [E_j^\pm]_{mn} &= \frac{-1}{P} \int_{P(S2)} dx \frac{e^{-ik_{jm}^\pm \cdot \vec{\rho}_s(x)}}{\sqrt{\beta_{jm}}} \exp \left[ik_{zi}x + i\frac{2n\pi}{P}x \right] \\ &= \frac{-1}{P\sqrt{\beta_{jm}}} \int_{P(S2)} dx \exp \left[-i(m-n)\frac{2\pi}{P}x - ik_{js}(\pm\beta_{jm})f_2(x) \right] \end{aligned} \quad (107)$$

$$[F_j^\pm]_{mn} = \alpha_{jn} [E_j^\pm]_{mn} \quad (108)$$

where (Sj) indicates that the integration is over surface j ,

$$a_{01n} = \delta_{n0} \sqrt{\beta_0} E_0 (\hat{e}_i \cdot \hat{y}) \quad (109)$$

and

$$a_{01n}^{(h)} = \delta_{n0} \sqrt{\beta_0} \frac{E_0}{\omega \mu} (\bar{k}_i \times \hat{e}_i \cdot \hat{y}) \quad (110)$$

The above \bar{a}_{01} elements are determined by the \hat{y} component of the incident electric and magnetic fields. Truncating the Fourier series of the surface field unknowns results in a finite matrix which can be inverted to obtain the surface field unknowns.

The integrals of the above matrix were evaluated exactly over a linearly interpolated sampled profile of the sinusoidal and quasi-sinusoidal surfaces.

Appendix B: MoM Matrix Equation

The matrix equation for the Method of Moments can be written as:

$$\begin{bmatrix} \bar{A} & c_2 \bar{B} & c_0 \bar{C} & 0 & 0 & 0 & 0 & 0 \\ -d_0 \bar{C} & 0 & \bar{A} & d_2 \bar{B} & 0 & 0 & 0 & 0 \\ \bar{D} & \bar{E} & 0 & 0 & \bar{F} & c_3 \bar{G} & c_1 \bar{H} & 0 \\ 0 & 0 & \bar{D} & \bar{E} & -d_1 \bar{H} & 0 & \bar{F} & d_3 \bar{G} \\ \bar{I} & \bar{J} & 0 & 0 & \bar{K} & c_3 \bar{L} & c_1 \bar{M} & 0 \\ 0 & 0 & \bar{I} & \bar{J} & -d_1 \bar{M} & 0 & \bar{K} & d_3 \bar{L} \\ 0 & 0 & 0 & 0 & \bar{N} & \bar{O} & 0 & 0 \\ 0 & 0 & 0 & 0 & 0 & 0 & \bar{N} & \bar{O} \end{bmatrix} \begin{bmatrix} \bar{a} \\ \bar{b} \\ \bar{c} \\ \bar{d} \\ \bar{e} \\ \bar{f} \\ \bar{g} \\ \bar{h} \end{bmatrix} = \begin{bmatrix} \bar{E}_{yi} \\ \bar{H}_{yi} \\ 0 \\ 0 \\ 0 \\ 0 \\ 0 \\ 0 \end{bmatrix} \quad (111)$$

where

$$[\bar{A}]_{mn} = \frac{\delta_{mn}}{2} + \int_{x_{n-1}(S1)}^{x_n} \hat{n}_1 \cdot \nabla_s G_{0P}(t_m, x) dS \quad (112)$$

$$[\bar{B}]_{mn} = \int_{x_{n-1}(S1)}^{x_n} G_{0P}(t_m, x) dx \quad (113)$$

$$[\bar{C}]_{mn} = G_{0P}(t_m, x_n) - G_{0P}(t_m, x_{n-1}) \quad (114)$$

$$[\bar{D}]_{mn} = \frac{\delta_{mn}}{2} - \int_{x_{n-1}(S1)}^{x_n} \hat{n}_1 \cdot \nabla_s G_{1P}(t_m, x) dS \quad (115)$$

$$[\bar{E}]_{mn} = - \int_{x_{n-1}(S1)}^{x_n} G_{1P}(t_m, x) dx \quad (116)$$

with the testing points and integration on surface one,

$$[\bar{F}]_{mn} = \int_{x_{n-1}(S2)}^{x_n} \hat{n}_1 \cdot \nabla_s G_{1P}(t_m, x) dS \quad (117)$$

$$[\bar{G}]_{mn} = \int_{x_{n-1}(S2)}^{x_n} G_{1P}(t_m, x) dx \quad (118)$$

$$[\bar{H}]_{mn} = G_{1P}(t_m, x_n) - G_{1P}(t_m, x_{n-1}) \quad (119)$$

with the testing points on surface one, integration on surface two,

$$[\bar{I}]_{mn} = - \int_{x_{n-1}(S1)}^{x_n} \hat{n}_1 \cdot \nabla_s G_{1P}(t_m, x) dS \quad (120)$$

$$[\bar{J}]_{mn} = - \int_{x_{n-1}(S1)}^{x_n} G_{1P}(t_m, x) dx \quad (121)$$

with the testing points on surface two, integration on surface one, and

$$[\bar{K}]_{mn} = \frac{\delta_{mn}}{2} + \int_{x_{n-1}(S2)}^{x_n} \hat{n}_1 \cdot \nabla_s G_{1P}(t_m, x) dS \quad (122)$$

$$[\overline{L}]_{mn} = \int_{x_{n-1}(S_2)}^{x_n} G_{1P}(t_m, x) dx \quad (123)$$

$$[\overline{M}]_{mn} = G_{1P}(t_m, x_n) - G_{1P}(t_m, x_{n-1}) \quad (124)$$

$$[\overline{N}]_{mn} = \frac{\delta_{mn}}{2} - \int_{x_{n-1}(S_2)}^{x_n} \hat{n}_1 \cdot \nabla_s G_{2P}(t_m, x) dS \quad (125)$$

$$[\overline{O}]_{mn} = \int_{x_{n-1}(S_2)}^{x_n} G_{2P}(t_m, x) dx \quad (126)$$

with the testing points and integration on surface two. The above integrals were approximated by a single point rectangular area at the testing point. This approximation becomes more accurate as the number of testing points is increased. In the results presented, 150 basis functions were used, which corresponds to 66 basis functions per wavelength in the free space region. This large number of basis functions was needed due to the much shorter wavelength in the high permittivity water region.

10 Figure Captions

Figure 1: Geometry of a "two-layer" periodic surface

Figure 2: Comparison of EBC and MOM brightness temperatures at polar angle 20° versus azimuthal angle (a) U_B (b) T_{Bh} (c) T_{Bv} (d) V_B

Figure 3: Measured brightness temperatures before and after noise removal calibration at polar angle 20° versus azimuthal angle (a) U_B (b) T_{Bh} (c) T_{Bv} (d) V_B

Figure 4: Measured brightness temperatures before and after noise removal calibration at polar angle 30° versus azimuthal angle (a) U_B (b) T_{Bh} (c) T_{Bv} (d) V_B

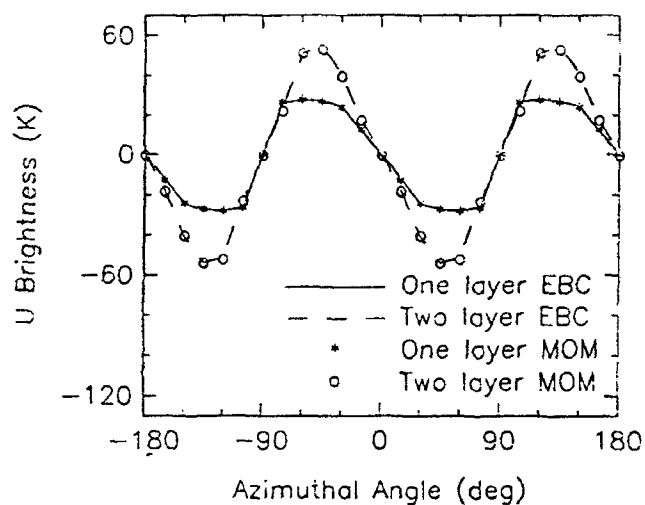
Figure 5: Comparison of theoretical and experimental brightness temperatures at polar angle 20° versus azimuthal angle (a) U_B (b) T_{Bh} (c) T_{Bv} (d) V_B

Figure 6: Comparison of theoretical and experimental brightness temperatures at polar angle 30° versus azimuthal angle (a) U_B (b) T_{Bh} (c) T_{Bv} (d) V_B

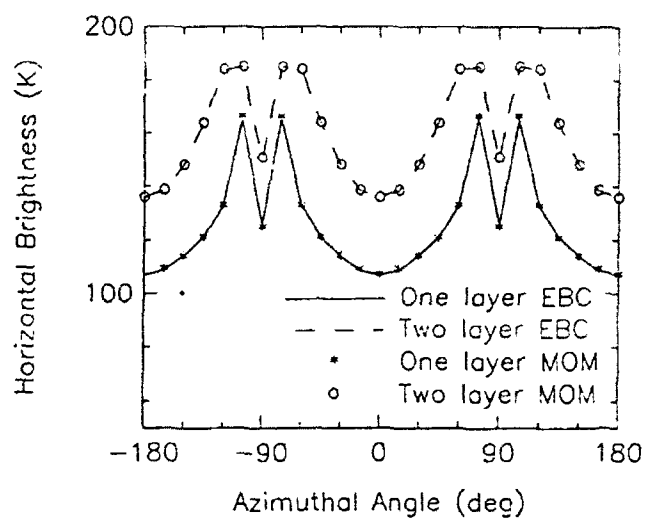
Figure 7: Comparison of beam averaged theoretical and experimental results for polar angle 20 degrees (a) U_B (b) T_{Bh} (c) T_{Bv} (d) T_{Bp}

Figure 8: Comparison of beam averaged theoretical and experimental results for polar angle 30 degrees (a) U_B (b) T_{Bh} (c) T_{Bv} (d) T_{Bp}

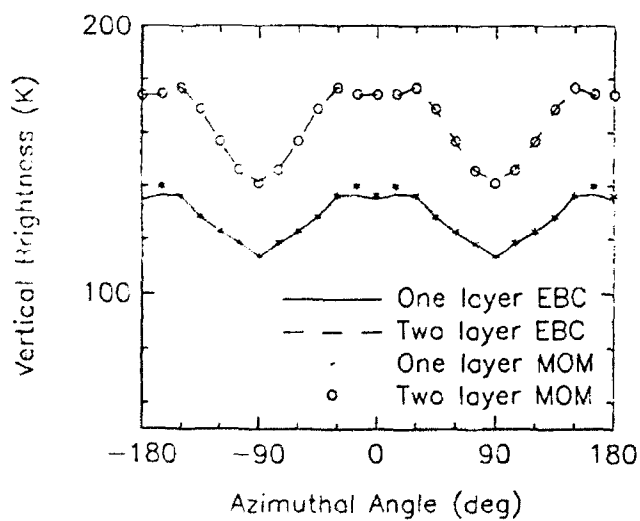
(a)



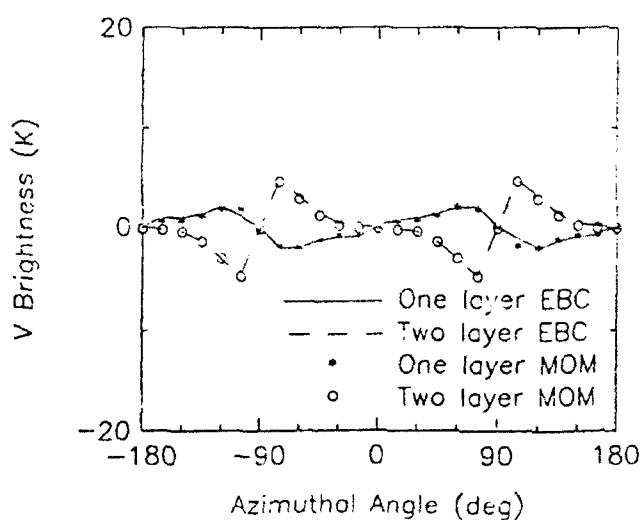
(b)



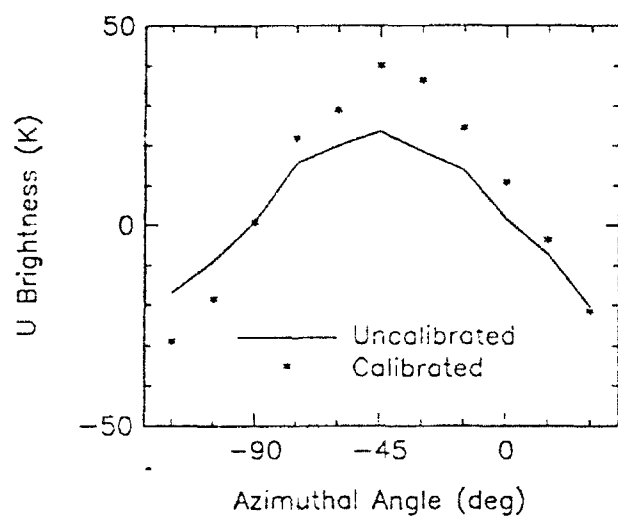
(c)



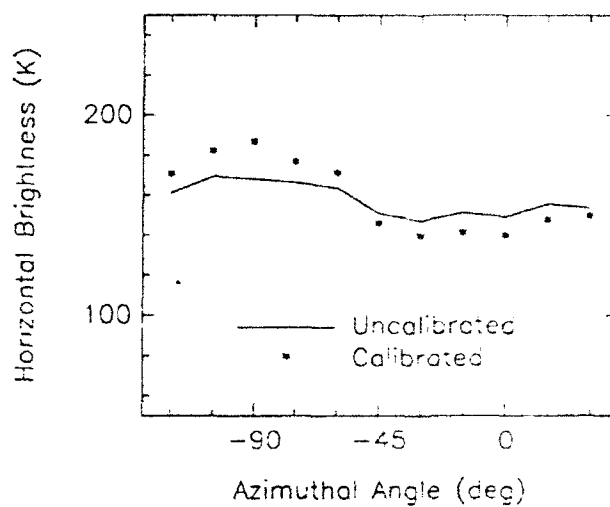
(d)



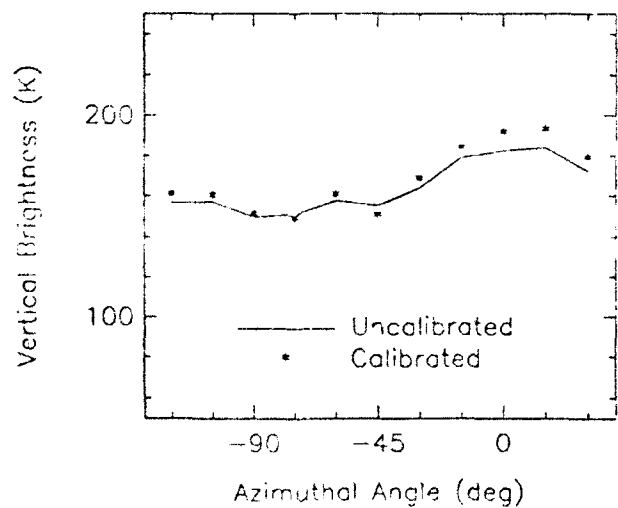
(a)



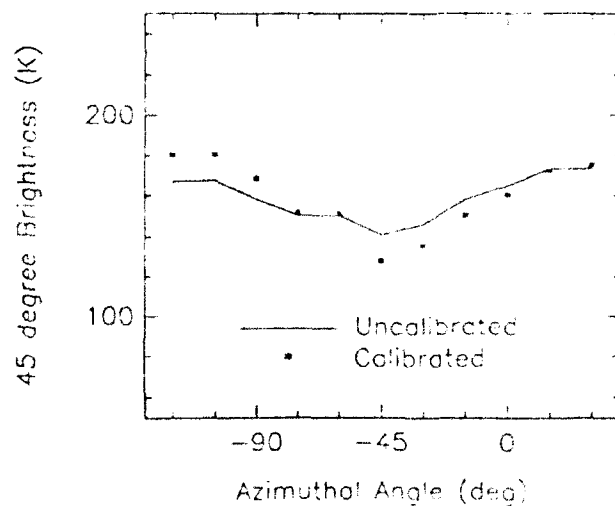
(b)



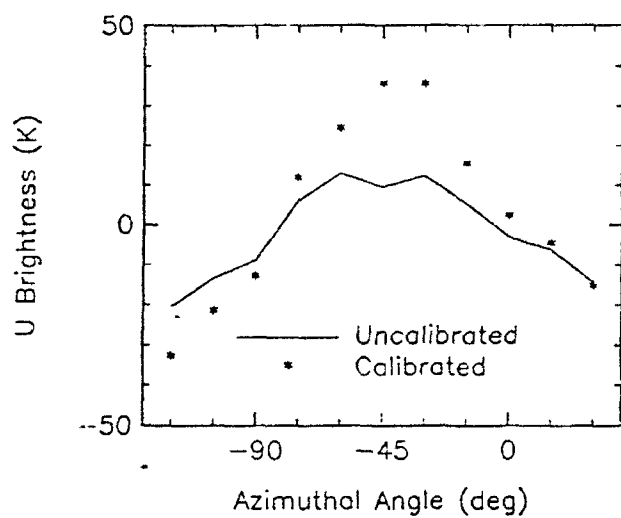
(c)



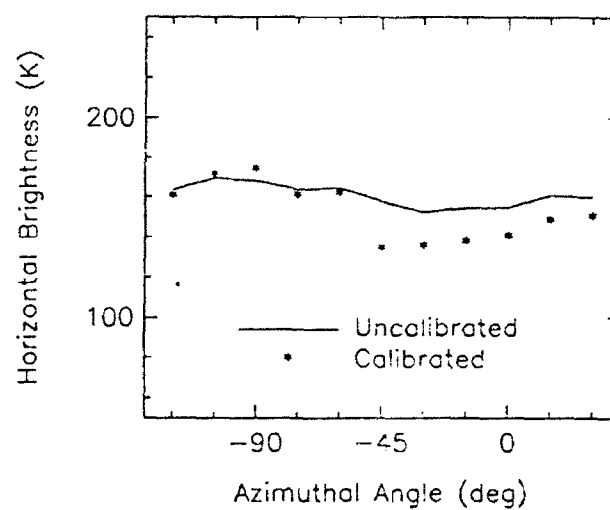
(c)



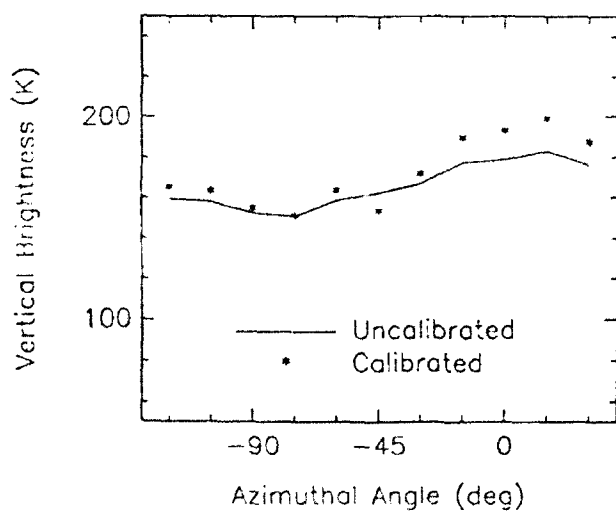
(a)



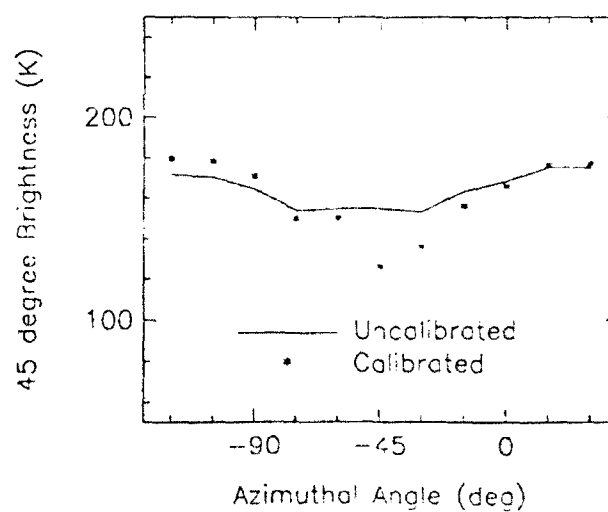
(b)

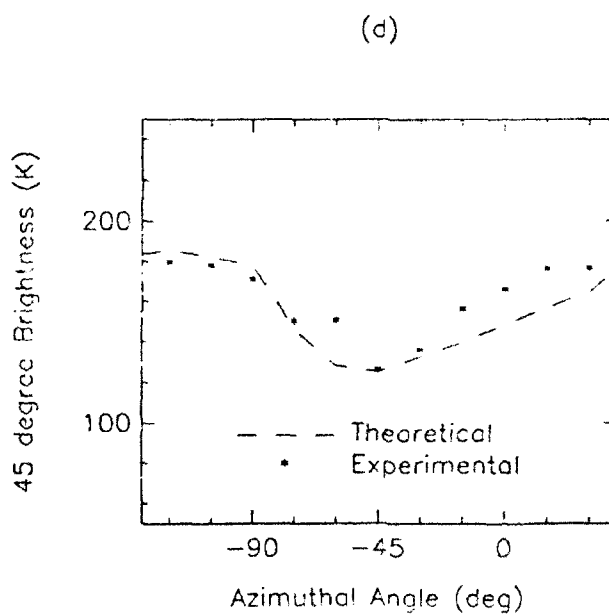
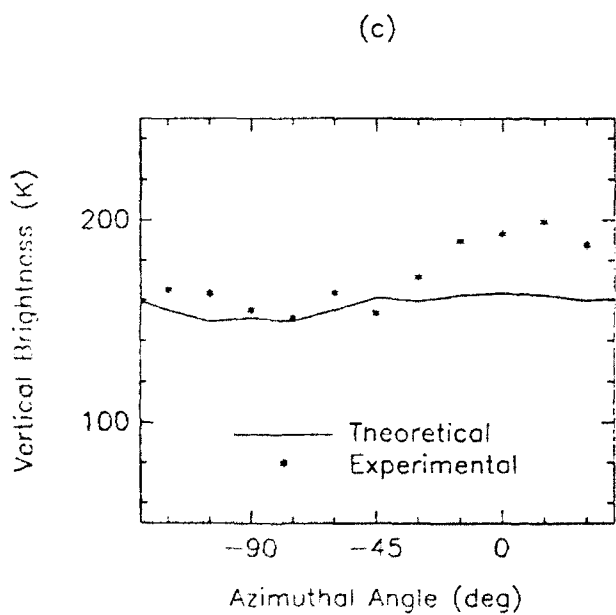
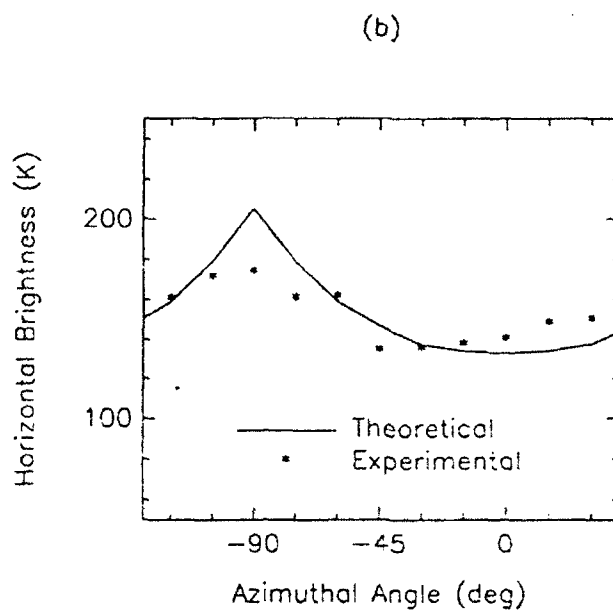
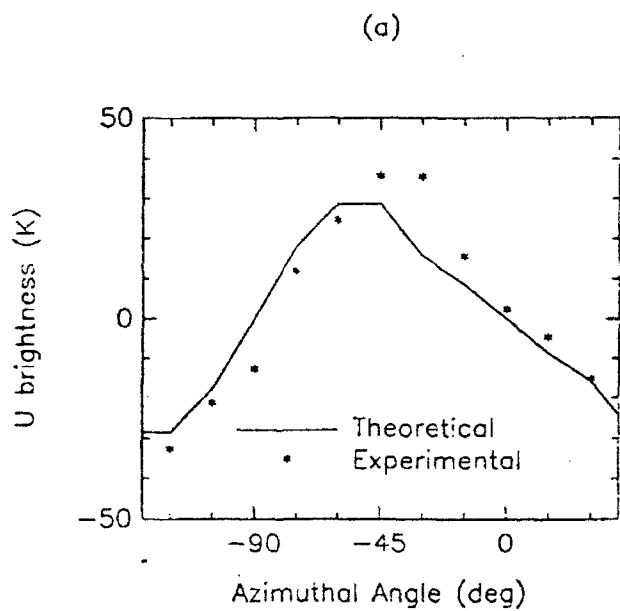


(c)

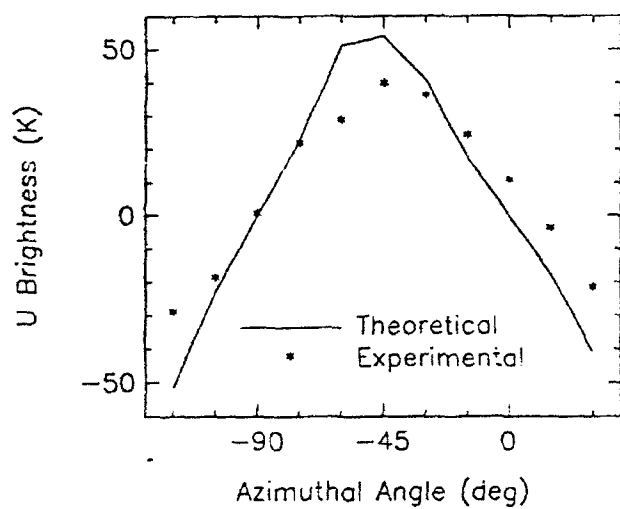


(d)

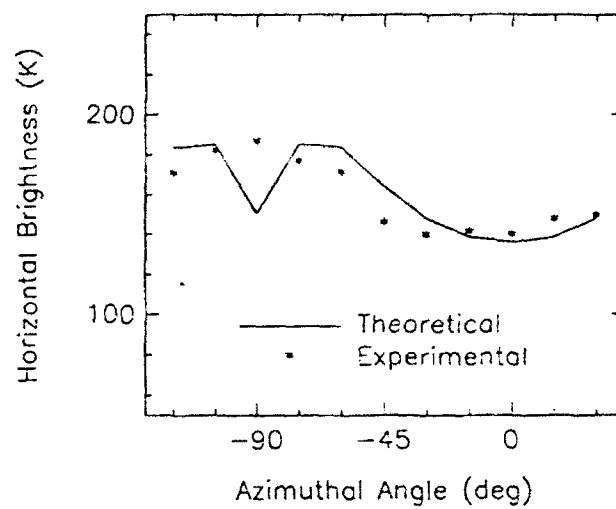




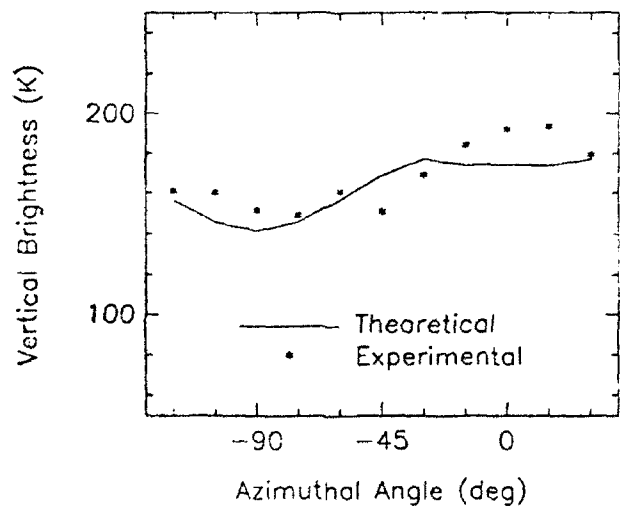
(a)



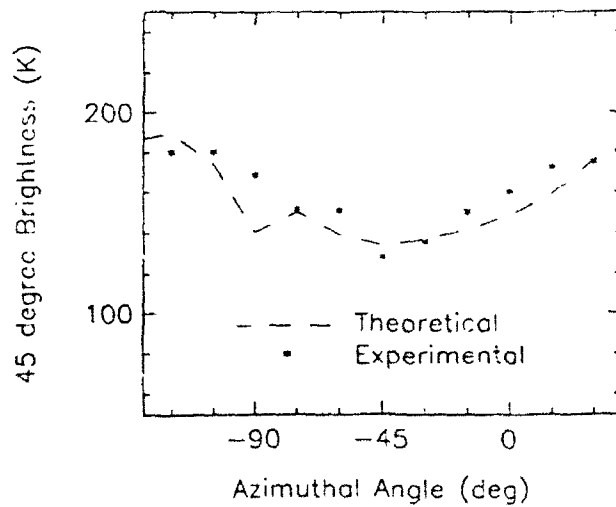
(b)



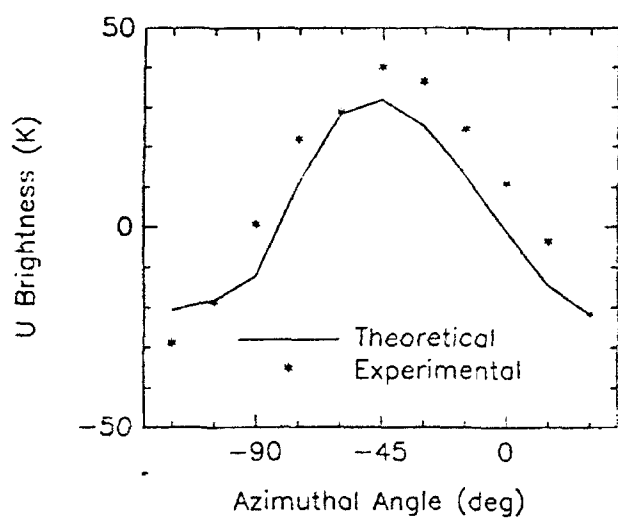
(c)



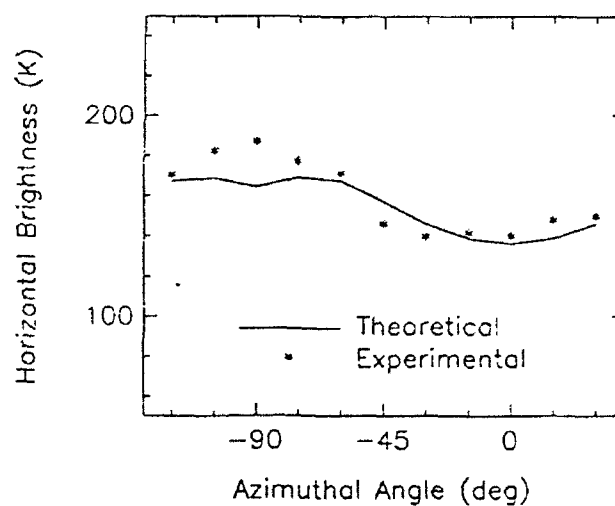
(d)



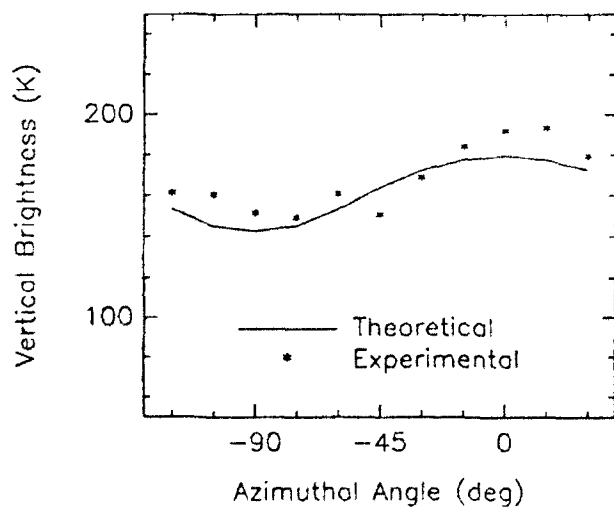
(a)



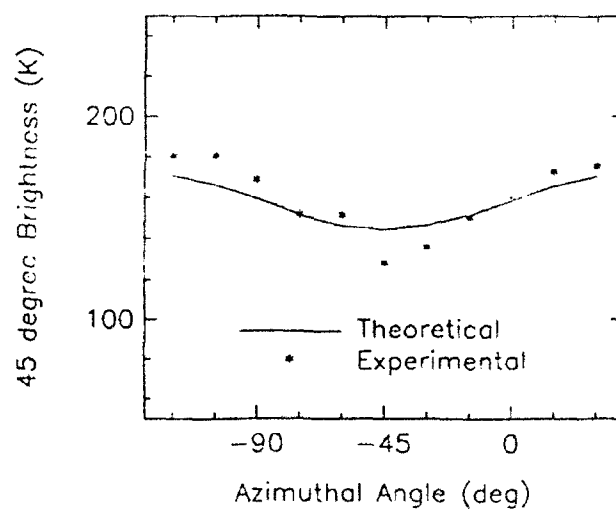
(b)



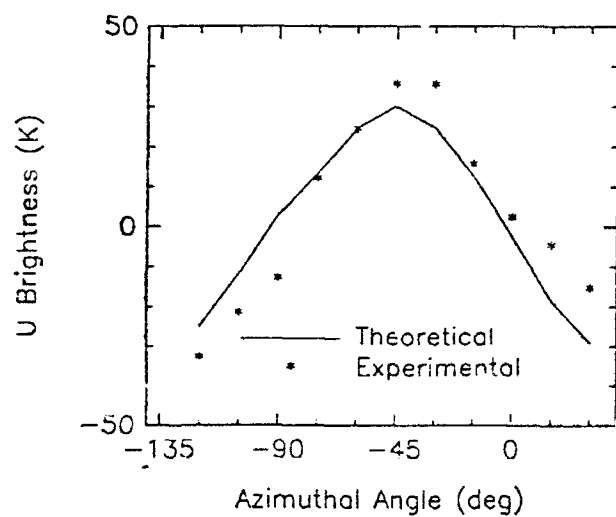
(c)



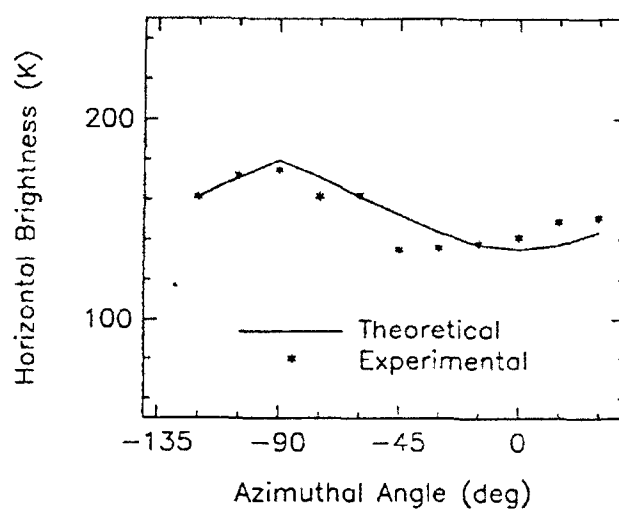
(d)



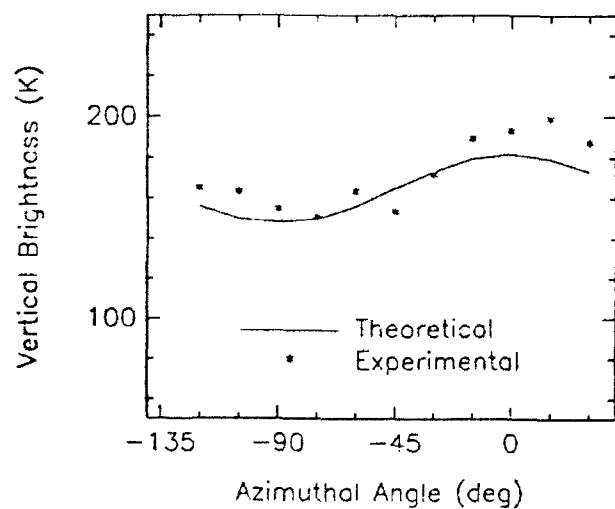
(a)



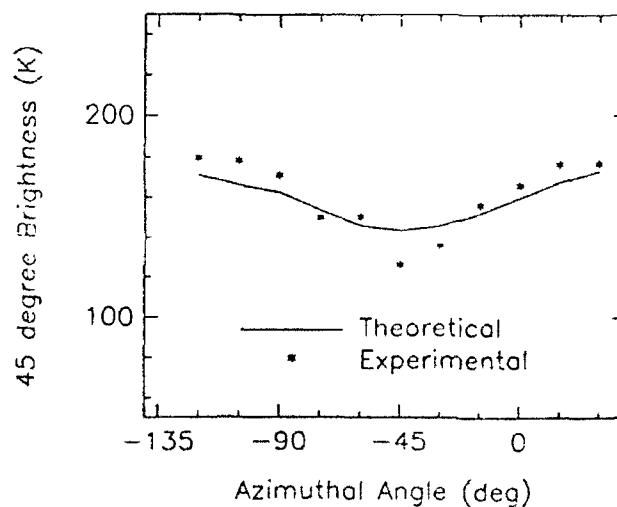
(b)



(c)



(d)



ATTACHMENT NUMBER 2REPORTS AND REPORTS DISTRIBUTIONREPORT TYPES

- (a) Performance (Technical) Report(s) (Include letter report(s))
Frequency: Annual
- (b) Final Technical Report, issued at completion of Grant.
- (c) Final Financial Status Report (SF 269)

REPORTS DISTRIBUTION

<u>ADDRESSEES</u>	<u>REPORT TYPES</u>	<u>NUMBER OF COPIES</u>
Scientific Officer Code: 1121RS Frank L. Herr Office of Naval Research 800 North Quincy Street Arlington, Virginia 22217-5000	(a) & (b)	3
Administrative Grants Officer Office of Naval Research Resident Representative Administrative Contracting Officer ONR MIT 495 Summer Street, Room 103 Boston, MA 02210-2109	(a) & (b) & (c)	1
Director, Naval Research Laboratory Attn: Code 2627 Washington, DC 20375	(a) & (b)	1
Defense Technical Information Center Building 5, Cameron Station Alexandria, Virginia 22304-6145	(a) & (b)	2

If the Scientific Officer directs, the Grantee shall make additional distribution of technical reports in accordance with a supplemental distribution list provided by the Scientific Officer. The supplemental distribution list shall not exceed 250 addresses.